https://doi.org/10.5194/egusphere-2025-2603
Preprint. Discussion started: 30 June 2025

The Sensitivity of Smoke Aerosol Dispersion to Smoke Injection Height and Source-Strength in Multiple AeroCom Models

Xiaohua Pan [1, 2], Mian Chin [2], Ralph A. Kahn [3,4], Hitoshi Matsui [5], Toshihiko Takemura[6], Meiyun Lin [7], Yuanyu Xie [8], Dongchul Kim [2,9], Maria Val Martin [10]

[1] ADNET systems, INC., Bethesda, MD, USA; [2] NASA Goddard Space Flight Center, Greenbelt, MD, USA; [3] Laboratory for Atmospheric & Space Physics, The University of Colorado, Boulder, USA; [4] Senior Research Scientist Emeritus, NASA GSFC, USA; [5] Nagoya University, Japan;[6] Kyushu University, Japan; [7] NOAA Geophysical Fluid Dynamics Laboratory, NJ, USA; [8]Princeton School of Public Policy and International Affairs, Princeton University, NJ, USA; A; [9] University of Maryland Baltimore County, USA; [10] School of Biosciences, University of Sheffield, UK

Correspondence to: Xiaohua Pan (xiaohua.pan@nasa.gov)

Abstract

The near-source and downwind impacts of smoke aerosols depend on both emitted mass and injection height. This study examines aerosol dispersion sensitivity to these factors using four global models from the AeroCom Phase III Biomass Burning Emission and Injection Height (BBEIH) experiment. Each model performed four simulations: (1) BASE, using a common emission inventory with default injection height; (2) BBIH, with vertical distribution adjusted using MISR plume heights; (3) BBEM, with an alternative emission inventory; and (4) NOBB, excluding biomass burning emissions. The focus is the April 2008 Siberian wildfire event. Aerosol optical depth (AOD) varied across models. The BASE model median is 27% higher than the satellite median over the Siberian wildfire source region but is 37% lower over the western North Pacific, indicating inadequate long-range transport or overly rapid aerosol removal in all models. Near the source, all models overestimate aerosol extinction below 2 km, suggesting injection heights were too low. The MISR plume heights slightly improved simulations, but downwind AOD remained largely underestimated. In BBEM, increased emissions in the models enhanced AOD near the source but did not improve AOD vertical structure there or downwind. Notably, CALIOP detected aerosol layers above 6 km from the source to downwind regions—features absent in all model simulations. These findings suggest that increasing emission strength alone is insufficient; improving vertical injection near-source to loft more smoke above 3 km in Siberia and reducing excessive aerosol wet removal during transport are critical.

1 Introduction

Smoke aerosols from wildfire can adversely affect air quality and visibility not only near the source locations (Konovalov et al., 2011; McCarty et al., 2017) but also in downwind regions hundreds or even thousands of kilometers away during transport. For example, smoke from the Siberia fire in Spring 2008 was found as far away as over Japan (e.g., Ikeda et al., 2015), the Arctic (Warneke et al., 2009), and

https://doi.org/10.5194/egusphere-2025-2603
Preprint. Discussion started: 30 June 2025

Canada (Cottle et al., 2014). Transported smoke can affect the near-source environment, e.g., the concentration of suspended sediment in a lake (Scordo et al., 2021) and can create air quality issues over extended areas (Liu et al., 2015, Xie et al., 2020; Lin et al., 2024). Wildfires can also impact surface albedo, air temperature, the atmospheric radiation field, cloud properties, and precipitation (Lu and Sokolik, 2013; Péré et al., 2014; Lee et al., 2022), and even stratospheric temperature and forcing (Stocker et al., 2021; Das et al., 2021).

The impact of smoke aerosols on the environments near the source and downwind depends not only on the emitted mass amount (or source strength) but also on factors such as injection height, chemical transformation, removal processes, and subsequent transport (Kahn et al., 2008; Paugam et al., 2016; Wilmot et al., 2022). This is especially true for large boreal forest fires that often emit smoke above the planetary boundary layer (PBL) into the free troposphere, and sometimes even into the lower stratosphere, where long-distance transport is more efficient (e.g., Val Martin et al., 2010, 2018; Peterson et al., 2018). Although some models use simple plume-rise parameterizations (Paugam et al., 2016, Lu et al., 2023) to estimate smoke injection height, most current atmospheric models operate under the assumption that fire emissions are primarily injected within the planetary boundary layer (PBL) or at altitudes below approximately 3 kilometers in the Aerosol Comparisons between Observations and Models (AeroCom) international initiative Phase-III study (e.g., Petrenko et al., 2025). This assumption potentially underrepresents the impact of high-intensity fires that loft emissions well above this level. Uncertainty in modeling the vertical smoke aerosol distribution in models has been reported in many studies and the issue persists (e.g., Koch et al., 2009, Chen et al., 2009, Koffi et al., 2012, Paugam et al., 2016, Vernon et al., 2018, Zhu et al., 2018; Tang et al., 2022, Li et al., 2023.)

This study reports the results on a multi-model experiment addressing the environmental effects of biomass burning (BB) emission and injection height on aerosol vertical profiles over the source and downwind areas for the Eurasia boreal region. This project, named Biomass Burning Emission Injection Height (BBEIH), is a part of the AeroCom international initiative Phase-III study (https://aerocom.met.no/node/110). The AeroCom BBEIH experiment is designed primarily to assess the impact of the smoke emission vertical profile. To assess the impact of fire emission injection height and source-strength for the major forest wildfires, we focus on the boreal fire case over Siberia and Kazakhstan in April 2008, which was the largest fire event in Russia during 2000-2008 in terms of total burned area, estimated from MODIS satellite observations (Vivchar, 2011). Long-range transport of the Siberia/Kazakhstan smoke was detected over Alaska during the NASA ARCTAS (Arctic Research of the Composition of the Troposphere from Aircraft and Satellites) and NOAA ARCPAC (Aerosol, Radiation, and Cloud Processes affecting Arctic Climate) field campaigns over Alaska in April 2008, with CO and aerosol concentrations above background levels enhanced by 100-300% (Warneke et al., 2009, 2010).

We compare model results using default smoke injection heights with those constrained by near-source plume-height observations from the Multi-Angle Imaging SpectroRadiometer (MISR) aboard NASA's Earth Observing System (Val Martin et al., 2010; 2018). This study addresses two key questions: 1) How sensitive are simulated near-source and downwind plume characteristics—including vertical

https://doi.org/10.5194/egusphere-2025-2603
Preprint. Discussion started: 30 June 2025

aerosol distribution, near-surface concentrations, and aerosol optical depth (AOD)—to the injection height of biomass burning emissions? and 2) To what degree does the choice of biomass burning emission inventory or source-strength affect smoke dispersion?

In the following sections, we first describe the AeroCom Phase III BBEIH model experiment in Sect. 2, then present the results in Sect. 3, discuss the results in Sect. 4, and finally, present the conclusions from this study in Sect. 5.

2. Overview of the AeroCom Phase III BBEIH experiment and analysis approach

In this section, we summarize the model runs performed and analyzed, the biomass burning emission inventories used, and the satellite aerosol amount and vertical distribution products used as constraints and for validation.

2.1 BBEIH model experiment

Table 1 lists the resolution, and the default fire emission vertical distribution schemes applied in the four models participating in the BBEIH project, i.e., the schemes used in their BASE experiments. The CAM5-ATRAS (or CAM5 in short) and the GFDL-AM4 (or GFDL) models followed the vertical distribution scheme from Dentener et al. (2006), in which large-scale wildfire emissions are distributed over six altitude ranges from 0 to 6 km according to wild-land fire location and type. For example, in temperate region, 30° - 60°N, BB emissions are distributed vertically as follows: 20% in 0-0.1 km, 20% from in 0.1-0.5 km, 20% in 0.5-1 km, 40% in 1-2 km, and zero for the remaining layers. Note that the fraction changes when the latitude is lower than 30°N and higher than 60°N. In the MIROC-SPRINTARS model (or SPRI), the BB emissions are injected between the surface and the altitude with a sigma level equal to 0.74 assuming a homogeneous mixing ratio (~the first 13 levels, approximately 3 km). In the GEOS-i33p2 model (or GEOS), BB emissions are distributed uniformly up to the top of the Planetary Boundary Layer, with a PBL height (or PBLH) about 0.68 km over boreal Eurasia.

Table 1. List of models and the default fire emission vertical distribution schemes in the BBEIH project

Model Name	**lon°×lat°× #lev**	**Default emission altitude in boreal Eurasia**	**Contact**	**References**
CAM5-ATRAS (or CAM5)	2.5°×1.9°×30	30° - 60° N: 20% in 0-0.1 km, 20% in 0.1-0.5 km, 20% in 0.5-1 km, 40% in 1-2 km	Hitoshi Matsui	*Matsui, 2017 and Matsui and Mahowald, 2017*
GEOS-i33p2 (or GEOS)	0.5°×0.5°×72	Globe: Uniformly distributed within PBL	Xiaohua Pan	*Chin et al., 2002; Colarco et al., 2010*
GFDL-AM4 (or GFDL)	1.25°×1°×49	30° - 60° N: 20% 0-0.1 km, 20% 0.1-0.5 km, 20% 0.5-1 km, 40% 1-2 km	Meiyun Lin, Yuanyu Xie	*Horowitz et al., 2020 ; Xie et al., 2020*

MIROC-SPRINTARS (or SPRI)	0.56°×0.56°× 40	Globe: Emitted between the surface and the altitude with the sigma level of 0.74, nearly 3 km, with the homogeneous their mixing ratio (~the first 13 levels)	Toshihiko Takemura	*Takemura et al., 2005 and 2009.*

The model configurations differ across models. The CAM5-ATRAS model simulates meteorological and chemical fields interactively, including precipitation and wet deposition processes. To better represent realistic meteorological conditions during the simulation period, temperature and wind fields in the free troposphere (pressure < 800 hPa) were nudged toward the Modern-Era Retrospective analysis for Research and Applications, Version 2 (MERRA-2) reanalysis. The GEOS model was run in "replay" mode, in which winds, pressure, moisture, and temperature are constrained by the MERRA-2 reanalysis meteorological data (Gelaro et al., 2017). This configuration enables realistic simulation of actual events, like a traditional offline chemistry transport model (CTM), while also incorporating full model physics, including radiation and moist processes. The GFDL AM4 model is driven by observed sea surface temperatures and sea ice distributions, with horizontal winds nudged toward those from the National Centers for Environmental Prediction (NCEP) reanalysis using a pressure-dependent nudging technique (Lin et al., 2012). Precipitation and temperature are simulated interactively within the model. In MIROC-SPRINTARS, horizontal wind, temperature, and surface pressure are nudged toward the European Centre for Medium-Range Weather Forecasts (ECMWF) Reanalysis v5 (ERA5) data. Precipitation is diagnosed using large-scale condensation and cumulus convection schemes, following Watanabe et al. (2011).

Table 2 summarizes the four experiments conducted by four models for the BBEIH project. 1) In BASE, i.e., the control run, all models used the burned-area-based BB emission from the GFED4.1s emission inventory (Giglio et al., 2013; Randerson et al., 2018), with the model-default biomass burning injection height (Table 1). Other emissions from anthropogenic and natural sources are also included. 2) BBIH (i.e., Biomass Burning Injection Height), same as BASE but BB emissions vertical distribution constrained by the MISR plume injection height weighting functions (Val Martin et al., 2010; 2018) to examine the effects of different emission height between BASE and BBIH on aerosol dispersion and vertical distribution. 3) BBEM, same as BASE but with daily BB emissions from the Fire Energetics and Emissions Research (FEER, Ichoku & Ellison, 2014) to test model's sensitivity to the choice of BB emission inventory. 4) NOBB, same as BASE but with BB emission turned off to isolate the aerosol from biomass burning sources. Accordingly, we derive the BB contribution as the difference between the BASE and NOBB runs.

Table 2. List of experiments in the BBEIH project

Experiment	Emissions	BB emission injection height
BASE	Anthropogenic: CMIP6 Biomass burning: GFED4.1s	Default in each model

	Natural (dust, sea-salt, volcanic, biogenic): choice by individual model	
BBIH	Same as BASE	MISR plume injection height
BBEM*	Anthropogenic and natural emissions: Same as BASE Biomass burning emissions: FEERv1.0-G1.2	Default in each model
NOBB	Anthropogenic and natural emissions: Same as BASE Biomass burning emissions: None.	N/A

**GFDL does not have this experiment.*

2.2. BB emissions and injection height

2.2.1 The target regions

Figure 1 highlights the six regions targeted in this study. KAZA (yellow box over Kazakhstan) and RUS1 (red box over northeastern Russia) represent the two primary BB source regions. The remaining four regions—RUS2 (magenta box over northeastern Russia), RUS3 (green box over northeastern Russia), PAC (blue box over North Pacific Ocean), and ALA (purple box over Alaska)—are located progressively downwind to the east.

2.2.2 BB emission inventories: GFED4.1s and FEER1.0

This study employs two biomass burning (BB) emission inventories—GFED4.1s (used in the BASE run) and FEER1.0 (used in the BBEM run)—to assess the sensitivity of aerosol distributions to differences in source strength and spatial allocation. Figure 1 compares their organic aerosol (OA) BB emissions for April 2008. GFED4.1s (top panel) shows lower OA emissions in both key source regions, KAZA and RUS1, compared to FEER1.0 (bottom panel). Regional total emissions for each of the six focus regions are also provided in Fig. 1. In KAZA, GFED4.1s reports total OA emissions of 106 kg s^{-1}—about one-quarter of those from FEER1.0. In RUS1, emissions are 578 kg s^{-1} in GFED4.1s and 702 kg s^{-1} (21% more) in FEER1.0. Across both inventories, BB emissions in RUS1, largely driven by forest fires, are substantially higher than in KAZA, where agricultural waste burning dominates. Notably, biomass burning activity in the Siberia–Lake Baikal region peaked in April 2008, exceeding levels observed in other months of the year (see Fig. A1).

GFED4.1s estimates total dry matter consumed by biomass burning by multiplying the MODIS burned area product at 500m spatial resolution (Giglio et al., 2010) with fuel consumption per unit burned area (van der Werf et al., 2017). The latter is the product of the fuel load per unit area and the combustion completeness. Then, species-specific emissions are derived using emission factor (EF, in grams of species per kilogram of dry matter burned) from Akagi et al. (2011), supplemented from Andreae and Merlet (2001). GFED4.1s considers small fires (Giglio et al., 2013; Randerson et al., 2012).

In comparison, the FEER1.0 (Ichoku and Ellison, 2014) calculates BB emissions based on the satellite detected Fire Radiative Power (FRP) from MODIS. More specifically, the BB aerosol emission rate is derived by multiplying ecosystem-specific emission coefficients (Ce) by MODIS FRP data that have been preprocessed and gridded in the GFAS1.2 analysis system (Kaiser et al., 2012). To derive the emission coefficients at pixel level within each grid cell, Ichoku and Ellison (2014) correlate the FRP for multiple cases with the plume AOD and area divided by the advection time (which is estimated from the apparent length of the plume in the MODIS imagery and a wind speed obtained from a reanalysis product). Ce corresponds to the slope of the linear regression fit. Then, the biomass burning emission of a given species is calculated by multiplying the ratio of that species with total particulate matter (TPM), based on the EF (Andreae and Merlet, 2001, with updates provided by Andreae, 2014). More information on the intercomparison of these two BB inventories can be found at Pan et al (2020).

2.2.3 MISR plume heights for 2008

Figure 2a reveals the spatial distribution of the percentage of the smoke emitted within the planetary boundary layer (or PBL) in April 2008 (units: %), derived from the MISR-retrieved plume injection height. The numerical values in Fig. 2a represent the area mean percentage of smoke column-abundance concentrated in the PBL in each of six targeted regions for April 2008. Figure 2b presents the vertical distribution of smoke emissions for April 2008 over the BB emission source region of KAZA and RUS1. The PBL, derived from MERRA-2 data, is shown in gray shading, with average PBL heights of approximately 0.77 km in KAZA and 0.68 km in RUS1. MISR-based plume height estimates indicate that only 53% of smoke in KAZA and 45% in RUS1 was injected within the PBL, as shown by the black cumulative profiles in Fig. 2b**.** For comparison, the default vertically cumulative fire emission profiles from the model BASE runs are also shown, with values summarized in Table 1. Among the models, only GEOS assigns 100% of fire emissions to the PBL. Both CAM5 and GFDL adopt the vertical distribution scheme from Dentener et al. (2006), resulting in identical vertical profiles in their BASE runs; below the PBL top, this scheme allocates a similar fraction of smoke as the MISR-based plume height estimates in KAZA and RUS1. However, above 2 km, it distributes less smoke than the MISR-based approach. In contrast, SPRI diverges significantly from the other three models, allocating more smoke above the PBL than any of the other models and the MISR-based results. Overall, nearly all smoke—close to 100%—is injected below 3 km in both KAZA and RUS1 across all distribution schemes, despite the observations showing smoke aerosols present above 3 km. This discrepancy is further discussed in Sect.3.4.

The MISR-retrieved plume injection height dataset shown in Fig. 2 is based on a climatology developed from the work of Val Martin et al. (2018; Table S4). This dataset provides regional, monthly AOD-weighted statistical summaries of plume heights, derived using the MISR INteractive eXplorer (MINX) tool (Nelson et al., 2013), with which thousands of individual smoke plumes observed in 2008 MISR data were analyzed. The resulting vertical profiles were gridded according to six land cover types across seven geographic regions. Although fire detections occurred only at specific locations, the derived profiles were applied across grids sharing the same land cover classification. It is assumed that, within each land cover region, the sampled plume profiles are representative of the entire region. This assumption is supported in part by statistical consistency across multiple cases within most land cover types.

The final product is a monthly gridded dataset (longitude, latitude, altitude) with a horizontal resolution of 0.25° and a vertical resolution of 250 m, spanning from the surface up to 6 km (25 altitude bins). It provides the vertical distribution of near-source biomass burning emissions. For the BBIH simulation, modelers interpolated or re-gridded this dataset to match their model's specific spatial and vertical resolution. The MISR-derived vertical AOD fractions were then multiplied by the corresponding GFED4.1s BB emissions at each model level.

The MINX software derives plume heights by assessing the parallax of contrast elements in multi-angle imagery from MISR's nine cameras, which acquire view angles ranging from 70 forward to 70 aft. The product has 1.1 km horizontal resolution and between 250 m and 500 m vertical resolution (Nelson et al., 2013). As it takes about seven minutes for all nine MISR cameras to image a given location on Earth, the proper motion of plume contrast elements is also obtained and is used to derive plume-level motion vectors, from which wind corrections are made to the geometrically retrieved heights.

MISR is in a sun-locked, near-polar orbit with a swath-width of about 380 km, so near-global coverage is obtained about once per week – about every eight days near the equator, and up to every two days near the poles (e.g., Diner et al., 1998). Equator crossing occurs at about 10:30 local time, so the typical late-afternoon peak in fire activity is not captured in the MISR observations.

2.3. Model Evaluation Datasets (MODIS, MISR, CALIOP)

We evaluated the simulated monthly AOD at 550 nm against three satellite datasets: MODIS, MISR, and CALIOP.

2.3.1 MODIS Aerosol Optical Depth

We used the AOD retrieved from the Level 3 monthly MODIS collection 6.1 products from the Terra and Aqua satellites from the combination of Dark Target (DT) (Remer et al., 2005; Levy et al., 2013) and Deep Blue (DB) (Hsu et al., 2013; Sayer et al., 2014) aerosol algorithms. The DT aerosol algorithm was designed for aerosol retrievals over land (mostly vegetated) and ocean surfaces that are dark in the visible (VIS) to shortwave infrared (SWIR) parts of the spectrum. The DB algorithm was designed for aerosol retrieval over brighter surfaces such as deserts, using shorter blue wavelengths.

2.3.2 MISR Aerosol optical depth

We used the version 23 monthly level 3 total AOD data at half-degree resolution and 558 nm wavelength from the MISR instrument on board the EOS Terra satellite (Kahn et al., 2010; Witek et al., 2019; Garay et al., 2020; MISR v23, with filename tagged as F15_0032), downloaded from the NASA Langley Atmospheric Sciences Data Center (ASDC) website https://asdc.larc.nasa.gov/project/MISR. The MISR product takes advantage of the nine view-angles acquired, ranging from 70˚ aft, through nadir, to 70˚ forward along the satellite orbit, at each of four wavelengths centered at 446, 558, 672, and 867 nm (Diner et al., 1998), to derive constraints on particle size, shape, and light-absorption along with AOD (Martonchik et al., 2009; Kahn & Gaitley, 2015).

2.3.3 CALIOP aerosol vertical profile

CALIOP is a two-wavelength backscatter lidar on board the Cloud-Aerosol Lidar and Infrared Pathfinder Satellite Observation (CALIPSO) satellite that has daily equator crossing times of about 13:30 and 01:30 and a 16-day repeating cycle. CALIOP measures directly the aerosol backscatter vertical profiles that are converted to aerosol extinction profile using assumed, aerosol type-dependent, lidar ratios (i.e., extinction-to-backscatter ratios) (Omar et al., 2009; Kim M.-H. et al., 2018). The mean extinction profiles of total aerosol are obtained from version 4.10 CALIOP Level 2 aerosol profile data with a nominal along-track resolution of 5 km and vertical resolution of 30 meters. We used the cloud-free, quality- assured, nighttime aerosol extinction profiles from CALIOP at 532 nm, developed by Kim D. et al. (2019). These cover Asia and the North Pacific regions with stricter cloud-aerosol-discrimination (CAD) scores of -100 to -70 (Yu et al. 2019) than the operational CAD score (-100 to -20, Tackett et al., 2018; Winker et al., 2013) to better ensure the aerosol data quality. These data were then averaged over a month and gridded into 5°×2° (longitude x latitude). The CALIOP AOD is obtained by integrating the vertical extinction profiles in the atmospheric column.

3. Results

In this section, we evaluate the model simulations of total-column AOD in the model simulations (Sect. 3.1), the sensitivity of total column-AOD to BB emission injection height and source-strength (Sect. 3.2), the sensitivity of aerosol surface concentration to BB emission injection height and source-strength (Sect. 3.3), and the sensitivity of vertical aerosol extinction profile to BB emission injection height and source-strength (Sect. 3.4).

3.1 Total-column AOD from satellite products and model simulations

Figure 3 presents the total-column AOD for April 2008 from satellite products (MODIS-Terra, MODIS-Aqua, MISR, and CALIOP), as well as from the BASE simulations and the difference between the BASE and NOBB simulations. Spatial distributions of AOD are shown in Fig. 3a, while Fig. 3b displays regional mean AOD values, calculated over non-missing data points. Aerosol measurements from MODIS and MISR cover only below 60 ºN due primarily to low sun angle and polar night. CALIOP, with its active lidar sensor, can provide aerosol observations under low-sun conditions and observe plumes up to 70º N latitude, although with sparser spatial sampling. Differences between MISR and MODIS AOD are evident, in part due to the broader spatial and temporal sampling of MODIS. The optically thick smoke plumes tend to be geographically small targets, and they are captured more frequently in the MODIS data record; this can be especially significant near source regions. AOD from CALIOP shows the highest AOD among the satellite products even though its spatial sampling is much less frequent than MODIS and MISR.

In Fig. 3a (first row), despite the limited availability of satellite aerosol retrievals at high latitudes, MODIS-Terra, MODIS-Aqua, MISR, and CALIOP all show high aerosol loading near Siberia-Lake

https://doi.org/10.5194/egusphere-2025-2603
Preprint. Discussion started: 30 June 2025

Baikal (RUS1) and in the downwind regions (RUS2, RUS3, and PAC). Additionally, pronounced aerosol loadings are observed in East Asia and South Asia. Enhanced AOD in Kazakhstan (KAZA) is evident across all four satellites. As shown in Fig. 3b, the regional-averaged AOD over KAZA ranges from 0.2 to 0.4, with MISR values about 40% lower than MODIS. Over RUS1, regional-averaged AODs range from 0.3 to 0.6 across the four satellites. Strong aerosol outflows from RUS1 toward RUS3 and PAC are clearly visible in MODIS, MISR, and CALIOP data, with area-averaged AODs between 0.4 and 0.5. The area-averaged AOD from CALIOP is 0.3 over ALA (Alaska). Measurements from the ARCPAC and ARCTAS field campaigns (Warneke et al., 2009; Matsui et al., 2011) observed transported smoke aerosol and high trace gas concentrations in ALA during April 2008.

The second row of Fig. 3a displays the total AOD simulated by the models in their BASE runs (CAM5, SPRI, GEOS, and GFDL), all using the GFED4.1s biomass burning emission inventory and the default smoke injection height settings. The corresponding biomass burning AOD (BASE minus NOBB) is shown in Fig. 3a (third row). Over the BB source regions, all BASE runs (second row of Fig. 3a) capture the high aerosol loading in RUS1, attributed to forest fires, and the slightly elevated AOD in KAZA due to agricultural fires (Warneke et al., 2009). However, the average model-simulated AODs differ significantly—by a factor of 2.8 over KAZA and 4.6 over RUS1, with CAM5 showing the lowest values (Fig. 3b). The model-simulated AOD is lower than the MODIS AOD over KAZA, with varying degrees of agreement over RUS1: CAM5 largely underestimates, GEOS and GFDL align better with MODIS observations, and SPRI largely overestimates. Over RUS2, the models simulate slightly higher AODs than RUS1, consistent with MODIS observations. In the RUS3 and PAC regions, all models underestimate AOD relative to MODIS observations, with an even larger underestimation observed in ALA.

Table 3 summarizes the medians of regional mean AOD from both satellite products and model simulations. Over the KAZA source region, the median AOD from the BASE model runs is only 52% of the satellite-derived median. In contrast, over RUS1, the BASE model median is 27% higher than the satellite median. Over PAC and ALA, the BASE model underestimates AOD by 37% and 65%, respectively. Figure 4 presents the normalized regional mean AOD from satellite observations and the BASE simulations. All BASE runs exhibit a steeper decline in AOD from RUS1 toward PAC compared to satellite data, indicating inadequate long-range transport or overly rapid aerosol removal in all models during transport. It should be noted that MISR shows anomalous behavior compared to MODIS in some regions, likely due to its sparse sampling coverage, which misses many short-lived, high-AOD plumes.

Table 3. The medians of regional mean AOD from satellites and model simulations

Median	**KAZA**	**RUS1**	**RUS2**	**RUS3**	**PAC**	**ALA**
Satellites	0.39	0.52	0.55	0.48	0.44	0.41
BASE	0.20	0.66	0.68	0.38	0.28	0.14
BBIH	0.20	0.64	0.66	0.39	0.29	0.15
BASE/Satellites	0.52	1.27	1.23	0.80	0.63	0.35
BBIH/Satellites	0.51	1.23	1.20	0.81	0.67	0.37

https://doi.org/10.5194/egusphere-2025-2603
Preprint. Discussion started: 30 June 2025

In RUS1, BB dominates the total AOD in the BASE runs, contributing to nearly 80% (Fig. 3b). Transported smoke from the RUS1 source region towards surrounding areas, for example, RUS2, RUS3, and PAC, is also significant in all models. However, the fraction of BB AOD is reduced as smoke plumes transport from the source to downwind regions; the longer the distance between the source and downwind region, the smaller the BB AOD fraction becomes. In RUS1, BB accounts for nearly from 70% (GFDL) to 92% (SPRI) of the extinction across all models. In RUS3, the contribution of BB is reduced, as might be expected, ranging from nearly 41% (GEOS) to 58% (CAM5), and is further reduced in PAC, ranging from 32% (GEOS)-38% (CAM5).

3.2 Sensitivity of total-column AOD to BB emission injection height and source-strength

The spatial distribution and regional mean AOD differences between the model sensitivity experiments and BASE runs are shown in Fig. 5, with spatial differences shown in Fig. 5a, and regional mean AOD differences in Fig. 5b. These results highlight the impact of constraining the fire plume injection height based on MISR retrievals and increasing the source-strength.

The AOD differences between BBIH and BASE (Fig. 5a, top row) extend from RUS1 to surrounding regions due to smoke transport but are generally small—within ±0.05 for most models and less than 0.01 in CAM5. These results indicate that model responses to changes in biomass burning injection height vary. All models except SPRI show reduced AOD in RUS1 and increased AOD in the outflow regions (RUS2, RUS3, and PAC) in the BBIH run compared to BASE, consistent with the differences in vertical profiles between the models' default profiles and the MISR-based profile (Fig. 2b). For example, GEOS exhibits the expected pattern: lower AOD in RUS1 and higher AOD downwind, consistent with 55% of emissions being injected above the PBL (0.68 km), facilitating greater long-range transport. Similarly, in the BBIH run, CAM5 and GFDL emit less biomass burning emissions below 2 km—90% compared to 100% in the BASE run. In contrast, SPRI shows the opposite behavior, with higher AOD in RUS1 and lower AOD downwind in BBIH relative to BASE. This is consistent with its vertical distribution in BBIH, which increased to nearly 90% the emissions confined within the first 2 km, compared to 70% in BASE (Fig. 2b), limiting transport.

Table 3 compares the medians of regional mean AOD from the BBIH and BASE simulations. Over the KAZA source region, the median AOD from the BBIH runs is similar to that from the BASE runs. In RUS1 and the downwind regions—RUS2, RUS3, PAC, and ALA—the BBIH medians are slightly closer to satellite-derived values, indicating that incorporating MISR plume injection heights generally improves AOD representation. However, these improvements are modest, typically ≤4%. This limited impact is attributed to differences in the default injection heights among models: GFDL and CAM5 already use injection heights similar to MISR, whereas SPRI injects too high and GEOS injects too low, resulting in minimal change in the multi-model median.

https://doi.org/10.5194/egusphere-2025-2603
Preprint. Discussion started: 30 June 2025

The overall increase in AOD from BASE to BBEM runs is shown spatially in Fig. 5a (bottom row), with regional mean differences summarized in Fig. 5b. Only three models—CAM5, GEOS, and SPRI—submitted BBEM simulations, which used FEER1.0 biomass burning (BB) emissions, whereas BASE runs used GFED4.1s. As shown in Fig. 1, GFED4.1s reports significantly lower OA BB emissions than FEER1.0: 106 kg s^{-1} in KAZA (about one-quarter of the FEER1.0 value) and 578 kg s^{-1} in RUS1 compared to 702 kg s^{-1} in FEER1.0. Consistent with the higher emissions, BBEM simulations produce significantly larger AODs than BASE, both near the source (e.g., +0.12 in RUS1) and downwind (e.g., +0.05 in RUS2 and +0.02 in RUS3).

As AOD represents only the integrated vertical column aerosol loading, sections 3.3 and 3.4 further examine the effects of biomass burning injection height and emission amount on surface aerosol concentration and vertical profiles, respectively.

3.3 Sensitivity of surface mass concentration to BB emission injection height and source-strength

The surface mass concentration of organic aerosols from biomass burning in BB runs across all four models are shown in Fig. 6 (first row). We find that biomass burning emissions produce enhanced surface mass concentrations near the source regions, up to 50 ug/m3 in KAZA and double in RUS1, especially in the GEOS model.

Figure 6 (second row) shows the difference in surface mass concentration of organic aerosols between the BBIH and BASE. In RUS1, CAM5, GEOS, and GFDL simulate reduced surface mass concentrations, up to 50 ug m^{-3}, and little changes toward the downwind regions. In contrast, SPRI shows the opposite response, indicating that BBIH leads to increased surface mass aerosols near the source region. This behavior is consistent results shown in Sect. 3.2, where we found that SPRI also produced more AOD near the source region in the BBIH run.

Figure 6 (third row) presents the difference between BBEM and BASE. Two models (CAM5 and GEOS5) show enhanced surface mass concentration in the BBEM run compared to BASE, both near the source and outflow regions. This is consistent with the enhanced AOD seen in the BBEM runs in Fig. 5, where the FEER inventory led to higher smoke aerosol loading in these two models.

Consistent what we found in Sect. 3.2 in terms of AOD, the differences of surface mass concentration of organic aerosols in BBIH of CAM5, GEOS, GFDL, and SPRI can be explained by the changes of BB emission profiles in their BBIH runs compared to their BASE runs (Fig. 2b).

3.4 Sensitivity of vertical aerosol extinction profile to BB emission injection height and source-strength

Figure 7 presents the vertical profiles of CALIOP aerosol extinction in April 2008, which is based on its backscatter measurements and their assumed extinction coefficients, along with the vertical profiles of four models' aerosol extinctions (CAM5, SPRI, GEOS, and GFDL) in four regions (from west to east: the source region RUS1, and three downwind regions, RUS3, PAC and ALA). Relevant statistics are listed next to the legend in each panel.

To evaluate the vertical profile, we used two vertical profile metrics, Z_a and $F_{2\,km}$.

$$Z_a = \frac{\sum_{i=1}^{k}(b_{ext,i} \ * \ Z_i)}{\sum_{i=1}^{k} b_{ext,i}}$$

Z_a represents the average aerosol layer height, following Koffi et al. (2012). Here k is the total number of layers in each column, $b_{ext,i}$ is the extinction coefficient for layer i within the column, and Z_i is the layer thickness for layer i. $F_{2\,km}$ is the AOD fraction in the lowest 2 km.

As shown in Fig. 7, in RUS1 (first column), CALIOP (thick black curves) has Z_a value of 2.74 km and $F_{2\,km}$ value of 51%. In the downwind RUS3 region (second column), CALIOP has a higher Z_a value of 3.5 km and F_{2km} drops to 34%, because parts of aerosol plumes below 2 km are removed while being transported to the downwind region. We found a similar trend in PAC (third column). Reaching to ALA (fourth column), F_{2km} increases to 40%, indicating that aerosol plumes descended toward the surface were further removed from the atmosphere.

Compared to CALIOP observations, all BASE runs (blue curves) consistently overestimate F_{2km} to varying degrees. For example, in the source region (RUS1), this overestimation ranges from 7% to 36% across models, suggesting that the models tend to overpredict aerosol loading in the lowest 2 km of the atmosphere. Similarly, in the downwind regions—RUS3 and PAC—the overestimations range from 6% to 17% and 10% to 22%, respectively, indicating that this high bias persists beyond the source region, and downwind smoke is distributed too close to the surface and/or descends too rapidly. Notably, CALIOP detects aerosol layers extending above 6 km from the source to downwind regions—features not reproduced by any of the models. As Fig. 2b shown, across all different schemes, nearly all smoke is injected only below 3 km in RUS1.

It is evident that biomass burning contributes significantly to the total extinction profiles in the source region (Fig. 7 and Fig. 3b), by comparing BASE (blue curves) and NOBB runs (orange curves) in each model. However, the contribution from BB becomes less towards the downwind regions. In addition, the simulated total aerosol extinction is reduced much more rapidly in RUS3, PAC, and ALA than observed by CALIOP, indicating that both biomass burning and non-biomass burning aerosols are removed from the models too quickly. In contrast, smoke originating from Siberia and Kazakhstan was still observed over Alaska during the April 2008 NASA ARCTAS and NOAA ARCPAC field campaigns. During this period, concentrations of carbon monoxide (CO) and aerosols were elevated by 100–300% above background levels (Warneke et al., 2009, 2010).

In the RUS1 region, the BBIH runs (red curves), where the smoke plume injection is constrained by MISR, brings three models (CAM5, GEOS, and GFDL) closer to CALIOP, with F_{2km} coming closer to the observed 51% by 9-17% across the three models. However, SPRI performs worse in this configuration, because the MISR-based vertical profile places a greater fraction of smoke below 2 km than the default vertical profile for this model (Fig. 2b). In the downwind regions (RUS3 and PAC), the BBIH runs show little improvement from BASE in any model.

The varying impact of BBIH across models reflects differences in their baseline (BASE) fire injection height schemes, as summarized in Table 1**.** In the BBIH run, all models adopted a consistent MISR-based vertical distribution: 45% of smoke is emitted within the PBL (~0.68 km), with the remainder above, following the MISR-derived weighting function **(**Fig. 2a and Sect. 2.2.3**).** The most significant improvement is observed in GEOS, where biomass burning emissions in the BASE run were confined entirely within the PBL. In contrast, the BBIH run injects 55% of emissions above the PBL, leading to improved agreement with observed vertical profiles in the RUS1 source region. Correspondingly, the fraction of aerosol extinction below 2 km ($F_{2\,km}$) decreases from 87% in BASE to 68% in BBIH.

CAM5 and GFDL use multi-level vertical profiles from Dentener et al. (2006) in their BASE runs. Switching to the MISR-based scheme in BBIH brings the fraction of AOD below 2 km (F2km) closer to the observed value of 51% in RUS1—decreasing from 65% to 59% in CAM5, and from 64% to 60% in GFDL (Fig. 7). This reduction helps explain the lower AOD in RUS1 seen in their BBIH simulations (Fig. 5a and 5b**).** This trend is consistent with their vertical profile comparisons in Fig. 2b.

The BBEM runs produced more BB emissions than BASE in three participating models (CAM5, GEOS, and SPRI), thus raising AOD near the source, yet not improving the vertical distribution or downwind AOD.

4. Discussion

4.1 BB AOD and emission discrepancies among models

To explore the sources of discrepancies among models, we examine the global spatial distribution of OA mass load (g m^{-2}), OA AOD, and OA mass extinction efficiency (MEE, $m^2\ g^{-1}$) for April 2008, as simulated by CAM5, SPRI, GEOS, and GFDL in their BASE runs (Fig. 8). The BBIH runs (not shown) resemble the BASE runs.

The global spatial patterns of OA mass load are broadly similar across the models, though SPRI displays more localized concentrations and less dispersion from source regions to surrounding areas (row 1 in Fig. 8). In contrast, OA AOD varies more substantially among the models, with CAM5 yielding notably lower values (row 2 in Fig. 8). These discrepancies are primarily driven by differences in MEE (row 3 in Fig. 8), as AOD is computed as the product of OA mass load and MEE. Due to extremely limited MEE measurements (e.g., Kahn et al., 2023), MEE is calculated within each model from species refractive indices, particle size distribution, particle density, and the RH-dependent hygroscopic growth. This leads to large diversity in model-adopted values. On both a global scale and within RUS1, GEOS and GFDL produce comparable MEE values, CAM5 the lowest, and SPRI the highest.

To further investigate the sources of variability in OA mass load, we analyzed global emissions of OA from biomass burning in April 2008 (Table 4). The BASE runs indicate that the global total organic carbon (OC) emissions from biomass burning are relatively consistent across the four models, ranging from 1.63 to 1.65 Tg. This consistency across models is confirmed in the global total black carbon (BC) biomass burning emission, ranging from 0.148-0.150 Tg (Table 5). However, substantial differences in the assumed OA/OC ratios—ranging from 1.4 to 2.6—lead to significant variations in total OA emissions in BASE, BBIH, and BBEM. The highest OA/OC ratio in SPRI (as 2.6) likely contributes to the overestimated AOD over RUS1 (Fig. 3a and 3b).

Table 4. Global OC Biomass burning emission for April 2008.

emibboa (Tg/mon) 200804	OA/OC ratio	BASE		BBIH		BBEM	
		OA	OC	OA	OC	OA	OC
CAM5	1.4	2.31	1.65	2.30	1.64	5.12	3.66
GEOS	1.8	2.95	1.64	2.91	1.62	6.62	3.68
GFDL	1.6	2.59	1.62	2.59	1.62	N/A	N/A
SPRI	2.6	4.23	1.63	4.23	1.63	9.54	3.67

Table 5. Global BC Biomass burning emission for April 2008.

emibbbc (Tg/mon) 200804	BASE	BBIH	BBEM
CAM5	0.150	0.149	0.384
GEOS	0.150	0.146	0.385
GFDL	0.148	0.148	N/A
SPRI	0.148	0.148	0.383

In summary, despite using identical biomass burning OC and BC emissions in the BASE simulations, the four models exhibit substantial variability in AOD and vertical aerosol profiles near the biomass burning source region (RUS1), as shown in Fig. 7. This variability is partly driven by the wide range of

https://doi.org/10.5194/egusphere-2025-2603
Preprint. Discussion started: 30 June 2025

OA/OC ratios assumed across models—ranging from 1.4 to 2.6—which results in significant differences in total OA emissions across the BASE, BBIH, and BBEM runs. Additionally, large inter-model differences in MEE further contribute to discrepancies in AOD and aerosol extinction. To improve future aerosol modeling and AeroCom intercomparisons, this study—along with Petrenko et al. (2025)—strongly recommends constraining OA/OC ratios and MEE values. However, the absence of systematic, region-specific measurements currently limits the ability to robustly constrain these parameters. Furthermore, the present analysis does not include the most extreme fire events, such as those associated with pyrocumulonimbus (PyroCb) development. Although beyond the scope of this study, such cases warrant further investigation, especially considering the projected increase in biomass burning intensity under a warming climate.

4.2 Removal processes in models

The total aerosol mass load in models is governed by a balance between sources—such as primary emissions and secondary aerosol formation—and removal processes, including dry deposition, wet deposition, and, to a lesser extent, chemical loss. As discussed in Sect.3, the models may be underestimating long-range transport or overestimating aerosol removal or both. To investigate this, we examine organic aerosol deposition in each model's BBIH run, where biomass burning emissions and the MISR-based vertical injection profile are held consistent across models.

Figure 9 illustrates the dry and wet deposition of OA in each model. The spatial patterns and magnitudes of OA dry deposition are generally consistent across models, showing a maximum over the RUS1 region and reduced deposition along the eastern coast of East Asia and northern South Asia—except too little in CAM5, which deviates from this pattern. In contrast, OA wet deposition is more widespread and stronger than dry deposition in all models, especially in CAM5. It spans regions including RUS1, RUS2, RUS3, PAC, and ALA, with decreasing intensity eastward.

These findings suggest that wet deposition is the dominant mechanism for OA removal across all models and likely contributes most to the excessive removal of biomass burning aerosols from the source regions to the downwind regions. However, in the current study we are unable to distinguish the effects of too rapid deposition from too inefficient transport.

5. Conclusions

This BBEIH study addresses two key questions: 1) How sensitive are simulated near-source and downwind plume characteristics—including vertical aerosol distribution, near-surface concentrations, and AOD—to the injection height of biomass burning emissions? and 2) To what degree does the choice of biomass burning emission inventory or source-strength affect smoke dispersion?

We evaluated the sensitivity of smoke aerosol dispersion to smoke injection height and source-strength in four global models. Each model performed four model simulation: In BASE, all models used the same biomass burning emission inventory (GFEDv4.1s) but with the model-specific BB injection height. In BBIH, the vertical distribution of biomass burning at injection was constrained by MISR plume injection height data, whereas in BBEM, the daily FRP-based biomass burning emission inventory (FEER) was used to assess model sensitivity to the emission dataset. In NOBB, BB emissions were excluded. This is the first AeroCom Phase III analysis to quantify inter-model variability in vertical smoke transport using MISR-constrained injection height.

In the BASE simulations, all models captured the AOD maximum associated with the Siberian wildfires near the Lake Baikal region in eastern Russia during April 2008. In the RUS1 region, biomass burning dominates AOD, contributing nearly 80% of the total. However, AOD levels varied notably among models: CAM5 significantly underestimates AOD, SPRI substantially overestimates it, whereas GEOS and GFDL show better agreement with MODIS observations. Despite this, all models consistently underestimated the strong aerosol outflow observed over the western North Pacific, where the satellite-derived median AOD is 0.44. The model ensemble median in this region is only 0.28, representing a 37% underestimation. In addition, All BASE simulations show a sharper decrease in AOD from RUS1 to PAC compared to satellite observations, suggesting that all models either have insufficient long-range aerosol transport or overestimate aerosol removal processes during transport. Compared to CALIOP, all models overestimated the fraction of AOD below 2 km (F2km), by 7–36% in RUS1 and downwind, by 6–17% in RUS3 and 10% to 22%, in PAC. Notably, CALIOP detects aerosol layers extending above 6 km from the source to downwind regions—these features not reproduced by any of the simulations. It indicates excessive smoke concentration near the surface across all models and overly rapid decrease during downwind transport.

In the BBIH run, all models applied a consistent MISR-based vertical distribution: 45% of smoke was emitted within the planetary boundary layer (~0.68 km) in the source region (RUS1), with the remainder above, following the MISR-derived weighting function. This led to a redistribution of AOD, surface OA mass concentration, and vertical profiles in most models. All models—except SPRI—showed reduced AOD in RUS1 and increased AOD in the outflow regions (RUS2, RUS3, and PAC) compared to the BASE run, although the changes were generally small—within ±0.05 for most models and less than 0.01 in CAM5. However, across all models, BBIH had limited impact on vertical smoke distribution in the downwind regions (RUS3 and PAC) and did not substantially reduce the persistent AOD underestimation there. The most notable improvement occurred in BBIH of GEOS, particularly in RUS1. The fraction of AOD below 2 km (F_{2km}) improved significantly in BBIH, decreasing from 87% in BASE to 68% in BBIH, closer to the CALIOP-observed value of 51%. This improvement reflects a shift from all BB emissions being confined within the PBL in the BASE run to 55% being injected above the PBL in BBIH. In summary, the default biomass burning injection heights in CAM5 and GFDL are relatively close to those retrieved by MISR, whereas GEOS assumes all emissions are injected within the PBL. As a result, the differences between the BASE and BBIH simulations are minimal for CAM5 and GFDL, while more noticeable improvements are observed in GEOS.

https://doi.org/10.5194/egusphere-2025-2603
Preprint. Discussion started: 30 June 2025

In SPRI, however, which uniformly distributes emissions up to 3 km in the BASE run, the BBIH scheme degrades agreement with observed AOD—this is because its default BB injection height is higher than MISR; using the MISR injection height would put more emission in the PBL (45-55%) than the default (22-25%) to increase the fraction below 1 km from 30% to 70%.

Across all vertical distribution schemes—including those adjusted using MISR plume heights—nearly all smoke, close to 100%, is injected below 3 km in both KAZA and RUS1. However, MISR observations (Val Martin et al., 2018), taken in the late morning (~10:30 a.m. local time), tend to underestimate typical peak daytime plume heights, as only about 20% of plumes rise above the boundary layer at that time, compared to ~55% by late afternoon (Ke et al., 2021). In addition, CALIOP detected aerosol layers above 6 km from the source to downwind regions—features absent in all model simulations. This highlights the need to inject more smoke above 3 km. Future modeling should consider how injection profiles might be adjusted to address this limitation and better represent plume rise above 3 km. Providing observations to adequately constrain aerosol transport models in this respect might require applying the combination of near-source injection height from multi-angle imaging (e.g. MISR and follow-on satellite missions), and downwind aerosol-plume vertical distribution (e.g., CALIOP and subsequent space-based aerosol lidars) (Kahn et al., 2008).

The FEER-based emission inventory (BBEM runs) resulted in higher biomass burning emissions—702 kg s^{-1} of OA compared to 578 kg s^{-1} in the GFED4.1s-based BASE runs for the RUS1 region. While this increase helped improve model-simulated AOD in the KAZA region, it led to an overestimation of AOD in RUS1 and RUS2. Additionally, the higher BB emissions did not enhance the vertical aerosol structure either locally or downwind, nor did they significantly increase AOD in downwind regions.

Lastly, model simulations of aerosol dispersion are essential tools for air quality forecasting and exposure assessment, as well as for climate prediction. Limitations in modeling, as indicated by diversity among models and discrepancies with available measurements, highlight the directions in which further advances are needed. Our results indicate that increasing biomass burning emission strength alone is insufficient to reproduce observed aerosol distributions. As with the discussion in Sect. 4 above, Petrenko et al. (2025) also found that different choices of MEE and OA/OC, along with differences in aerosol loss rate, played a major role in creating diversity among model BB AOD and discrepancies with MODIS AOD, including simulations produced by the CAM5, GEOS, and SPRI models also applied in the current study. Equally critical is to quantitatively assess the efficiencies of transport, in both vertical and horizontal dimensions, and of removal of aerosols, which would require implementation of common diagnostic tracers in the models. These considerations are important for better understanding the model simulated smoke near the source and downwind and how to make improvements and should help the design of the upcoming AeroCom Phase IV experiments. Further, there is a lack of critical measurements for constraining particle microphysical properties such as MEE and aerosol properties and processes such as OA/OC ratio, loss rates, and aerosol vertical distribution that would be required to make the implied model adjustments consistently and appropriately (e.g., Kahn et al., 2023).

https://doi.org/10.5194/egusphere-2025-2603
Preprint. Discussion started: 30 June 2025

Appendix A

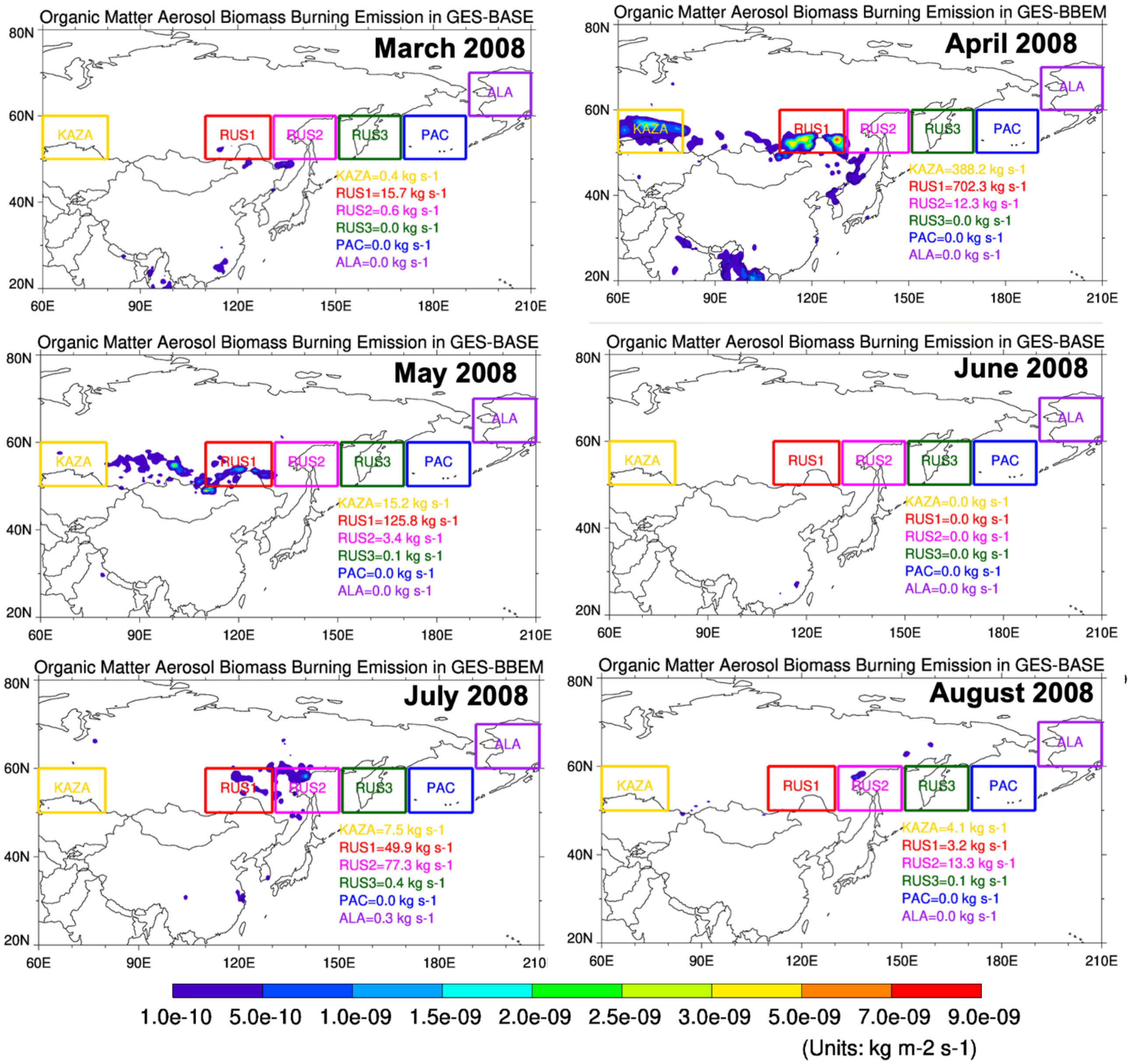

Figure A1. Spatial distribution of monthly mean organic matter aerosol emissions from biomass burning from March to August 2008, based on the GFED4.1s inventory (from the GEOS BASE run), in units of kg m^{-2} s^{-1}. The six focus regions are highlighted, with total emissions indicated for each region.

Author contribution

MC, XP, and RK conceived this project. XP conducted the data analysis and the model experiments. MC also conducted the data analysis. XP, RK, and MC wrote most of this paper, and all other authors participated in the revising process and interpretation of the results. HM, TT, ML, and YX also conducted model experiments. DK and MM provided the datasets and interpretation of these datasets.

Competing interests

At least one of the co-authors is a member of the editorial board of Atmospheric Chemistry and Physics.

Code/Data availability

The model simulation outputs from the AeroCom Phase III Biomass Burning Emission and Injection Height (BBEIH) experiment used in this study are available upon request from the corresponding author or through the AeroCom database (https://aerocom.met.no/). The MISR plume height data and CALIOP aerosol profiles used for evaluation are publicly available from NASA's Earthdata portal (https://earthdata.nasa.gov/). Custom analysis scripts are available upon reasonable request.

Disclaimer

The contents of this article are solely the responsibility of the authors and do not represent the official views of any agency or institution.

Acknowledgements

We thank the MODIS, MISR, and CALIOP teams for making their AOD data available. Computing resources supporting this work were provided by the NASA High-End Computing (HEC) Program through the NASA Center for Climate Simulation (NCCS) at the Goddard Space Flight Center. We also thank the providers of biomass burning emission datasets of GFED and FEER. Xiaohua Pan also acknowledges the valuable suggestions from Hongbin Yu on the CALIOP data.

Financial support

The work of X. Pan, M. Chin, and D. Kim is supported by NASA MAP program. The work of R. Kahn is supported in part by NASA's Terra-Aqua-Suomi NPP program and the Terra/MISR project. T. Takemura was supported by the Environment Research and Technology Development Fund S-20 (grant no. JP-MEERF21S12010) of the Environmental Restoration and Conservation Agency provided by the Ministry of the Environment, Japan, and NEC SX-Aurora TSUBASA at National Institute for Environmental Studies, Japan. H. Matsui was supported by the MEXT/JSPS KAKENHI Grand Numbers JP23H00515, JP23H00523, JP23K18519, JP23K24976, and JP24H02225, the MEXT Arctic Challenge for Sustainability Phase II (ArCS II; grant no. JPMXD1420318865) project, the Environment Research and Technology Development Fund 2–2301 (JPMEERF20232001) of the Environmental

Restoration and Conservation Agency, and National Institute of Polar Research (NIPR) through Special Collaboration Project no. B25-02. M. Val Martin acknowledges funding from the UKRI Future Leaders Fellowship Programme (MR/T019867/1).

References

Akagi, S. K., Yokelson, R. J., Wiedinmyer, C., Alvarado, M. J., Reid, J. S., Karl, T., Crounse, J. D., and Wennberg, P. O.: Emission factors for open and domestic biomass burning for use in atmospheric models, Atmos. Chem. Phys., 11, 4039–4072, https://doi.org/10.5194/acp-11-4039-2011, 2011.

Andreae, M. O. and Merlet, P.: Emission of trace gases and aerosols from biomass burning, Global Biogeochem. Cy., 15, 955–966, https://doi.org/10.1029/2000GB001382, 2001.

Chen, Y., Li, Q., Randerson, J. T., Lyons, E. A., Kahn, R. A., Nelson, D. L., and Diner, D. J.: The sensitivity of CO and aerosol transport to the temporal and vertical distribution of North American boreal fire emissions, Atmos. Chem. Phys., 9, 6559–6580, https://doi.org/10.5194/acp-9-6559-2009, 2009.

Chin, M., Ginoux, P., Kinne, S., Torres, O., Holben, B. N., Duncan, B. N., Martin, R. V., Logan, J. A., Higurashi, A., and Nakajima, T.: Tropospheric aerosol optical thickness from the GOCART model and comparisons with satellite and sun photometer measurements, J. Atmos., Sci., 59, 461–483, 2002.

Colarco, P. R., da Silva, A., Chin, M., and Diehl, T.: Online simulations of global aerosol distributions in the NASA GEOS-4 model and comparisons to satellite and groundbased aerosol optical depth, J. Geophys. Res., 115, D14207, https://doi.org/10.1029/2009JD012820, 2010.

Cottle, Paul, Kevin Strawbridge, and Ian McKendry. “Long-range transport of Siberian wildfire smoke to British Columbia: Lidar observations and air quality impacts.” Atmospheric environment 90 (2014): 71-77.

Das, S., Colarco, P. R., Oman, L. D., Taha, G. & Torres, O. The long-term transport and radiative impacts of the 2017 British Columbia pyrocumulonimbus smoke aerosols in the stratosphere. Atmos. Chem. Phys. 21, 12069–12090 (2021).

Dentener, F., J. Drevet, J.F. Lamarque, I. Bey, B. Eickhout, A.M. Fiore, D. Hauglustaine, L.W. Horowitz, M. Krol, U.C. Kulshrestha, M. Lawrence, C. Galy-Lacaux, S. Rast, D. Shindell, D. Stevenson, T. Van Noije, C. Atherton, N. Bell, D. Bergman, T. Butler, J. Cofala, B. Collins, R. Doherty, K. Ellingsen, J. Galloway, M. Gauss, V. Montanaro, J.F. Müller, G. Pitari, J. Rodriguez, M. Sanderson, F. Solmon, S. Strahan, M. Schultz, K. Sudo, S. Szopa, and O. Wild, 2006: Nitrogen and sulfur deposition on regional and global scales: A multimodel evaluation. *Glob. Biogeochem. Cycles*, 20, GB4003, doi:10.1029/2005GB002672.

Diner, D.J., J.C. Beckert, T.H. Reilly, C.J. Bruegge, J.E. Conel, R.A. Kahn, J.V. Martonchik, T.P. Ackerman, R. Davies, S.A.W. Gerstl, H.R. Gordon, J-P. Muller, R. Myneni, R.J. Sellers, B. Pinty, and M.M. Verstraete, 1998. Multiangle Imaging SpectroRadiometer (MISR) description and experiment overview, *IEEE Trans. Geosci. Remt. Sensing 36*, 1072-1087, doi: 10.1109/36.700992.

Garay, M.J., M.L. Witek, R.A. Kahn, F.C. Seidel, J.A. Limbacher, M.A. Bull, D.J. Diner, E.G. Hansen, O.V. Kalashnikova, H. Lee, A.M. Nastan, and Y. Yu, 2020. Introducing the 4.4 km Spatial Resolution MISR Aerosol Products. Atm. Meas. Tech. 13, 593-628, doi.org/10.5194/amt-13-593-2020.

Gelaro, R., McCarty, W., Suárez, M. J., Todling, R., Molod, A., Takacs, L., Randles, C. A., Darmenov, A., Bosilovich, M. G., Reichle, R., Wargan, K., Coy, L., Cullather, R., Draper, C., Akella, S., Buchard, V., Conaty, A., da Silva, A. M., Gu, W., Kim, G., Koster, R., Lucchesi, R., Merkova, D., Nielsen, J. E., Partyka, G., Pawson, S., Putman, W., Rienecker, M., Schubert, S. D., Sienkiewicz, M., and Zhao, B.: The Modern-Era Retrospective Analysis for Research and Applications, Version 2 (MERRA-2), J. Climate, 30, 5419–5454, https://doi.org/10.1175/JCLI-D-16-0758.1, 2017.

Giglio, L., Randerson, J. T., van der Werf, G. R., Kasibhatla, P. S., Collatz, G. J., Morton, D. C., and DeFries, R. S.: Assessing variability and long-term trends in burned area by merging multiple satellite fire products, Biogeosciences, 7, 1171–1186, https://doi.org/10.5194/bg-7-1171-2010, 2010.

Giglio, L., J. T. Randerson, and G. R. van derWerf (2013), Analysis of daily, monthly, and annual burned area using the fourth-generation global fire emissions database (GFED4), J. Geophys. Res. Biogeosci. 118, 317–328, doi:10.1002/jgrg.20042.

Horowitz, L. W., Naik, V., Paulot, F., Ginoux, P. A., Dunne, J. P., & Mao, J., et al. (2020). The GFDL global atmospheric chemistry-climate model AM4.1: Model description and simulation characteristics. Journal of Advances in Modeling Earth Systems, 12, e2019MS002032. https://doi.org/10.1029/2019MS002032.

Hsu, N.C., M.J. Jeong, C. Bettenhausen, A.M. Sayer, R. Hansell, C.S. Seftor, J. Huang, and S.-C. Tsay, 2013. Enhanced Deep Blue aerosol retrieval algorithm: The second generation, J. Geophys. Res. Atmos., 118, 9296–9315, doi:10.1002/jgrd.50712.

Ichoku, C. and L. Ellison (2014). Global top-down smoke-aerosol emissions estimation using satellite fire radiative power measurements. Atmos. Chem. Phys., 14, 6643–6667, doi: 10.5194/acp-14-6643-2014.

Ikeda, K., & Tanimoto, H. (2015). Exceedances of air quality standard level of PM2. 5 in Japan caused by Siberian wildfires. Environmental Research Letters, 10(10), 105001.

Kahn, R. A., Chen, Y., Nelson, D. L., Leung, F. Y., Li, Q., Diner, D. J., & Logan, J. A. (2008). Wildfire smoke injection heights: Two perspectives from space. Geophysical Research Letters, 35(4).

Kahn, R.A., B.J. Gaitley, M.J. Garay, D.J. Diner, T. Eck, A. Smirnov, and B.N. Holben, 2010. Multiangle Imaging SpectroRadiometer global aerosol product assessment by comparison with the Aerosol Robotic Network. J. Geophys. Res. 115, D23209, doi:10.1029/2010JD014601.

Kahn, R.A., and B. J. Gaitley, 2015. An analysis of global aerosol type as retrieved by MISR. J. Geophys. Res. Atmos. 120, 4248-4281, doi:10.1002/2015JD023322.

Kahn, R.A., E. Andrews, C.A. Brock, M. Chin, G. Feingold, A. Gettelman, R.C. Levy, D.M. Murphy, A. Nenes, J.R. Pierce, T. Popp, J. Redemann, A.M. Sayer, A. da Silva, L. Sogacheva, and P. Stier, 2023. Reducing Aerosol Forcing Uncertainty by Combining Models with Satellite and Within-the-Atmosphere Observations: A Three-Way Street. *Rev. Geophys. ROG20303*, doi:10.1029/2022RG000796.

Ke, Z., Wang, Y., Zou, Y., Song, Y., & Liu, Y.-Q. (2021). Global wildfire plume-rise dataset and parameterizations for climate model applications. *Journal of Geophysical Research: Atmospheres*, *126*(6), e2020JD033085. https://doi.org/10.1029/2020JD033085.

Koch, D., Schulz, M., Kinne, S., McNaughton, C., Spackman, J. R., Balkanski, Y., Bauer, S., Berntsen, T., Bond, T. C., Boucher, O., Chin, M., Clarke, A., De Luca, N., Dentener, F., Diehl, T., Dubovik, O., Easter, R., Fahey, D. W., Feichter, J., Fillmore, D., Freitag, S., Ghan, S., Ginoux, P., Gong, S., Horowitz, L., Iversen, T., Kirkevåg, A., Klimont, Z., Kondo, Y., Krol, M., Liu, X., Miller, R., Montanaro, V., Moteki, N., Myhre, G., Penner, J. E., Perlwitz, J., Pitari, G., Reddy, S., Sahu, L., Sakamoto, H., Schuster, G., Schwarz, J. P., Seland, Ø., Stier, P., Takegawa, N., Takemura, T., Textor, C., van Aardenne, J. A., and Zhao, Y.: Evaluation of black carbon estimations in global aerosol models, Atmos. Chem. Phys., 9, 9001–9026, https://doi.org/10.5194/acp-9-9001-2009, 2009.

Kim D. et al. 2019. "Asian and Trans-Pacific Dust: A Multimodel and Multiremote Sensing Observation Analysis." Journal of Geophysical Research: Atmospheres 2019JD030822 [10.1029/2019jd030822]

Koffi, B., Schulz, M., Bréon, F.-M., Griesfeller, J., Winker, D., Balkanski, Y., Bauer, S., Berntsen, T., Chin, M., Collins, W.
Dentener D., F., Diehl, T., Easter, R., Ghan, S., Ginoux, P., Gong, S., Horowitz, L. W., Iversen, T., Kirkevåg, A., Koch, D., Krol, M., Myhre, G., Stier, P., and Takemura, T.: Application of the CALIOP

layer product to evaluate the vertical distribution of aerosols estimated by global models: Aero-Com phase I results, J. Geophys. Res.-Atmos., 117, D10201, https://doi.org/10.1029/2011jd016858, 2012.

Konovalov, I. B., Beekmann, M., Kuznetsova, I. N., Yurova, A., and Zvyagintsev, A. M.: Atmospheric impacts of the 2010 Russian wildfires: integrating modelling and measurements of an extreme air pollution episode in the Moscow region, Atmos. Chem. Phys., 11, 10031–10056, https://doi.org/10.5194/acp-11-10031-2011, 2011.

Lee, J. Y., Peterson, P. K., Vear, L. R., Cook, R. D., Sullivan, A. P., Smith, E., et al. (2022). Wildfire smoke influence on cloud water chemical composition at Whiteface Mountain, New York. Journal of Geophysical Research: Atmospheres, 127, e2022JD037177. https://doi.org/10.1029/2022JD037177.

Levy, R. C., S. Mattoo, L. A. Munchak, et al. 2013. "The Collection 6 MODIS Aerosol Products over Land and Ocean." Atmos Meas Tech, 6: 2989-3034 [10.5194/amt-6-2989-2013].

Li, Y., D. Tong, S. Ma, S.R. Freitas, R. Ahmadov, M. Sofiev, X. Zhang, S. Kondragunta, R.A. Kahn, Y. Tang, B. Baker, P. Campbell, R. Saylor, I. Stajner, and G. Grell, 2022. Impacts of estimated plume rise on PM2.5 exceedance prediction during extreme wildfire events: A comparison of three schemes (Briggs, Freitas, Sofiev). Atmosph. Chem. Phys. 23, 3083–3101, doi:10.5194/acp-23-3083-2023.

Lin, M., Fiore, A. M., Horowitz, L. W., Cooper, O. R., Naik, V., Holloway, J., ... & Dlugokencky, E. J. (2012). Transport of Asian ozone pollution into surface air over the western United States in spring. *Journal of Geophysical Research: Atmospheres*, *117*(D00V07). https://doi.org/10.1029/2011JD016961.

Lin, M., L. W. Horowitz, Lu Hu, Wade Permar. Reactive nitrogen partitioning enhances the contribution of Canadian wildfire smoke plumes to U.S. ozone air quality. Geophysical Research Letters, 51, e2024GL109369, https://doi.org/10.1029/2024GL109369, 2024.

Liu, J. C., Pereira, G., Uhl, S. A., Bravo, M. A., & Bell, M. L. (2015). A systematic review of the physical health impacts from non-occupational exposure to wildfire smoke. Environmental research, 136, 120-132.

Lu, Z., & Sokolik, I. N. (2013). The effect of smoke emission amount on changes in cloud properties and precipitation: A case study of Canadian boreal wildfires of 2007. Journal of Geophysical Research: Atmospheres, 118(20), 11-777.

Lu, Z., Liu, X., Ke, Z., Zhang, K., Ma, P.-L., & Fan, J. (2023). Incorporating an interactive fire plume-rise model in the DOE's Energy Exascale Earth System Model Version 1 (E3SMv1) and examining aerosol radiative effect. *Journal of Advances in Modeling Earth Systems, 16*(1), e2023MS003818. https://doi.org/10.1029/2023MS003818.

Martonchik, J.V., R.A. Kahn, and D.J. Diner, 2009. Retrieval of Aerosol Properties over Land Using MISR Observations. In: Kokhanovsky, A.A. and G. de Leeuw, ed., Satellite Aerosol Remote Sensing Over Land. Springer, Berlin, pp.267-293. ISBN 978-3-540-69396-3.

Matsui, H., et al. (2011), Seasonal variation of the transport of black carbon aerosol from the Asian continent to the Arctic during the ARCTAS aircraft campaign, J. Geophys. Res., 116, D05202, doi:10.1029/2010JD015067.

Matsui, H. **(**2017). Development of a global aerosol model using a two-dimensional sectional method: 1. Model design. *Journal of Advances in Modeling Earth Systems*, **9**(2), 900–937. https://doi.org/10.1002/2017MS000936.

Matsui, H., & Mahowald, N. M. **(2017**). Development of a global aerosol model using a two-dimensional sectional method: 2. Evaluation and sensitivity simulations. *Journal of Advances in Modeling Earth Systems*, **9**(2), 938–972. https://doi.org/10.1002/2017MS000937.

McCarty, J. L., Krylov, A., Prishchepov, A. V., Banach, D. M., Tyukavina, A., Potapov, P., & Turubanova, S. (2017). Agricultural fires in European Russia, Belarus, and Lithuania and their impact on air quality, 2002–2012. Land-Cover and Land-Use Changes in Eastern Europe after the Collapse of the Soviet Union in 1991, 193-221.

Nelson, D.L., M.J. Garay, R.A. Kahn, and B.A. Dunst, 2013. Stereoscopic Height and Wind Retrievals for Aerosol Plumes with the MISR INteractive eXplorer (MINX). *Remote Sens. 5*, 4593-4628, doi:10.3390/rs5094593.

Pan, X., Ichoku, C., Chin, M., Bian, H., Darmenov, A., Colarco, P., Ellison, L., Kucsera, T., da Silva, A., Wang, J. and Oda, T., 2020. Six global biomass burning emission datasets: intercomparison and application in one global aerosol model. Atmospheric Chemistry and Physics, 20(2), pp.969-994.

Paugam, R., Wooster, M., Freitas, S., & Val Martin, M. (2016). A review of approaches to estimate wildfire plume injection height within large-scale atmospheric chemical transport models. Atmospheric Chemistry and Physics, 16(2), 907-925.

Péré, J. C., Bessagnet, B., Mallet, M., Waquet, F., Chiapello, I., Minvielle, F., Pont, V., and Menut, L.: Direct radiative effect of the Russian wildfires and its impact on air temperature and atmospheric dynamics during August 2010, Atmos. Chem. Phys., 14, 1999–2013, https://doi.org/10.5194/acp-14-1999-2014, 2014.

Peterson, D.A., J.R. Campbel, E.J. Hyer, M.D. Fromm, G.P. Kablick, J.H. Cossuth, and M.T. DeLand, 2018. Wildfire-driven thunderstorms cause a volcano-like stratospheric injection of smoke. *npj Climate and Atmospheric Science 1:30*, doi:10.1038/s41612-018-0039-3.

Petrenko, M., Kahn, R., Chin, M., Bauer, S. E., Bergman, T., Bian, H., Curci, G., Johnson, B., Kaiser, J. W., Kipling, Z., Kokkola, H., Liu, X., Mezuman, K., Mielonen, T., Myhre, G., Pan, X., Protonotariou, A., Remy, S., Skeie, R. B., Stier, P., Takemura, T., Tsigaridis, K., Wang, H., Watson-Parris, D., and Zhang, K.: Biomass burning emission analysis based on MODIS aerosol optical depth and AeroCom multi-model simulations: implications for model constraints and emission inventories, Atmos. Chem. Phys., 25, 1545–1567, https://doi.org/10.5194/acp-25-1545-2025, 2025.

Randerson, J. T., Chen, Y., van der Werf, G. R., Rogers, B. M., and Morton, D. C.: Global burned area and biomass burning emissions from small fires, J. Geophys. Res.-Biogeo., 117, G04012, https://doi.org/10.1029/2012JG002128, 2012.

Randerson, J.T., G.R. van der Werf, L. Giglio, G.J. Collatz, and P.S. Kasibhatla. 2018. Global Fire Emissions Database, Version 4, (GFEDv4). ORNL DAAC, Oak Ridge, Tennessee, USA. Doi.org/10.3334/ORNLDAAC/1293.

Scordo, F., Chandra, S., Suenaga, E., Kelson, S. J., Culpepper, J., Scaff, L., ... & Poulson, S. R. (2021). Smoke from regional wildfires alters lake ecology. Scientific Reports, 11(1), 10922.

Stocker, M., Ladstädter, F., & Steiner, A. K. (2021). Observing the climate impact of large wildfires on stratospheric temperature. Scientific reports, 11(1), 22994.

Tang, W., Emmons, L. K., Buchholz,R. R., Wiedinmyer, C., Schwantes, R.H., He, C., et al. (2022). Effects of fire diurnal variation and plume rise on U.S. air quality during FIREX-AQ and WE-CAN based on the Multi-Scale Infrastructure for Chemistry and Aerosols (MUSICAv0). Journal of Geophysical Research: Atmospheres,127, e2022JD036650. https://doi.org/10.1029/2022JD036650.

Tackett, J. L., Winker, D. M., Getzewich, B. J., Vaughan, M. A., Young, S. A., & Kar, J. (2018). CALIPSO lidar level 3 aerosol profile product: Version 3 algorithm design. Atmospheric Measurement Techniques, 11, 4129–4152. https://doi.org/10.5194/amt-11-4129-2018.

Takemura, T., Nozawa, T., Emori, S., Nakajima, T. Y., and Nakajima, T.: Simulation of climate response to aerosol direct and indirect effects with aerosol transport-radiation model, J. Geophys. Res.-Atmos., 110, 1–16, https://doi.org/10.1029/2004JD005029, 2005.

Takemura, T., Egashira, M., Matsuzawa, K., Ichijo, H., O'ishi, R., and Abe-Ouchi, A.: A simulation of the global distribution and radiative forcing of soil dust aerosols at the Last Glacial Maximum, Atmos. Chem. Phys., 9, 3061–3073, https://doi.org/10.5194/acp-9-3061-2009, 2009.

Val Martin, M., J.A. Logan, R.A. Kahn, F-Y. Leung, D. Nelson, and D. Diner, 2010. Smoke injection heights from fires in North America: analysis of 5 years of satellite observations. Atm. Chem. Phys. 10, 1491-1510, doi: 10.5194/ACP-10-1491-2010.

Val Martin, M. R.A. Kahn, and M. Tosca, 2018. A Global Climatology of Wildfire Smoke Injection Height Derived from Space-based Multi-angle Imaging. Remote Sensing; 10, 1609, doi:10.3390/rs10101609.

van der Werf, G. R., Randerson, J. T., Giglio, L., van Leeuwen, T. T., Chen, Y., Rogers, B. M., Mu, M., van Marle, M. J. E., Morton, D. C., Collatz, G. J., Yokelson, R. J., and Kasibhatla, P. S.: Global fire emissions estimates during 1997–2016, Earth Syst. Sci. Data, 9, 697–720, https://doi.org/10.5194/essd-9-697-2017, 2017 (data available at: http://www.globalfiredata.org, last access: 17 January 2020).

Vernon, C.J., R. Bolt, T. Canty, and R.A. Kahn, 2018. The impact of MISR-derived injection-height initialization on wildfire and volcanic plume dispersion in the HySPLIT model. Atmosph. Meas. Tech. 11, 6289–6307, doi:10.5194/amt-11-6289-2018.

Vivchar, A. (2011). Wildfires in Russia in 2000–2008: estimates of burnt areas using the satellite MODIS MCD45 data. Remote Sensing Letters, 2(1), 81-90.

Watanabe, S., Hajima, T., Sudo, K., Nagashima, T., Takemura, T., Okajima, H., Nozawa, T., Kawase, H., Abe, M., Yokohata, T., Ise, T., Sato, H., Kato, E., Takata, K., Emori, S., and Kawamiya, M.: MIROC-ESM 2010: model description and basic results of CMIP5-20c3m experiments, Geosci. Model Dev., 4, 845–872, https://doi.org/10.5194/gmd-4-845-2011, 2011.

Warneke, C., Bahreini, R., Brioude, J., Brock, C. A., De Gouw, J. A., Fahey, D. W., ... & Veres, P. (2009). Biomass burning in Siberia and Kazakhstan as an important source for haze over the Alaskan Arctic in April 2008. Geophysical Research Letters, 36(2).

Warneke, C., et al. (2010), An important contribution to springtime Arctic aerosol from biomass burning in Russia, Geophys. Res. Lett., 37, L01801, doi:10.1029/2009GL041816.

Wilmot, T. Y., Mallia, D. V., Hallar, A. G., & Lin, J. C. (2022). Wildfire plumes in the Western US are reaching greater heights and injecting more aerosols aloft as wildfire activity intensifies. Scientific reports, 12(1), 12400.

Winker, D. M., Tackett, J. L., Getzewich, B. J., Liu, Z., Vaughan, M. A., and Rogers, R. R.: The global 3-D distribution of tropospheric aerosols as characterized by CALIOP, Atmos. Chem. Phys., 13, 3345–3361, https://doi.org/10.5194/acp-13-3345-2013, 2013.

https://doi.org/10.5194/egusphere-2025-2603
Preprint. Discussion started: 30 June 2025

Witek, M. L., Garay, M. J., Diner, D. J., & Smirnov, A. (2019). Oceanic aerosol loading derived from MISR's 4.4 km (V23) Aerosol Product. J. Geophys. Res.: Atmospheres, 124. doi:10.1029/2019JD031065.

Xie, Y., Lin, M., & Horowitz, L. W. (2020). Summer PM2.5 pollution extremes caused by wildfires over the western United States during 2017–2018. Geophysical Research Letters, 47, e2020GL089429. https://doi.org/10.1029/2020GL089429.

Yu H., Q. Tan, M. Chin, et al. 2019. "Estimates of African Dust Deposition Along the Trans-Atlantic Transit Using the Decadelong Record of Aerosol Measurements from CALIOP, MODIS, MISR, and IASI." Journal of Geophysical Research: Atmospheres 124 (14): 7975-7996 [10.1029/2019jd030574].

Zhu, L., M. Val Martin, A. Hecobian, M.N. Deeter, L.V. Gatti, R.A. Kahn, and E.V. Fischer, 2018. Development and implementation of a new biomass burning emissions injection height scheme for the GEOS-Chem model. *Geosci. Model Develop. 11, 4103–4116*, doi:10.5194/gmd-11-4103-2018.

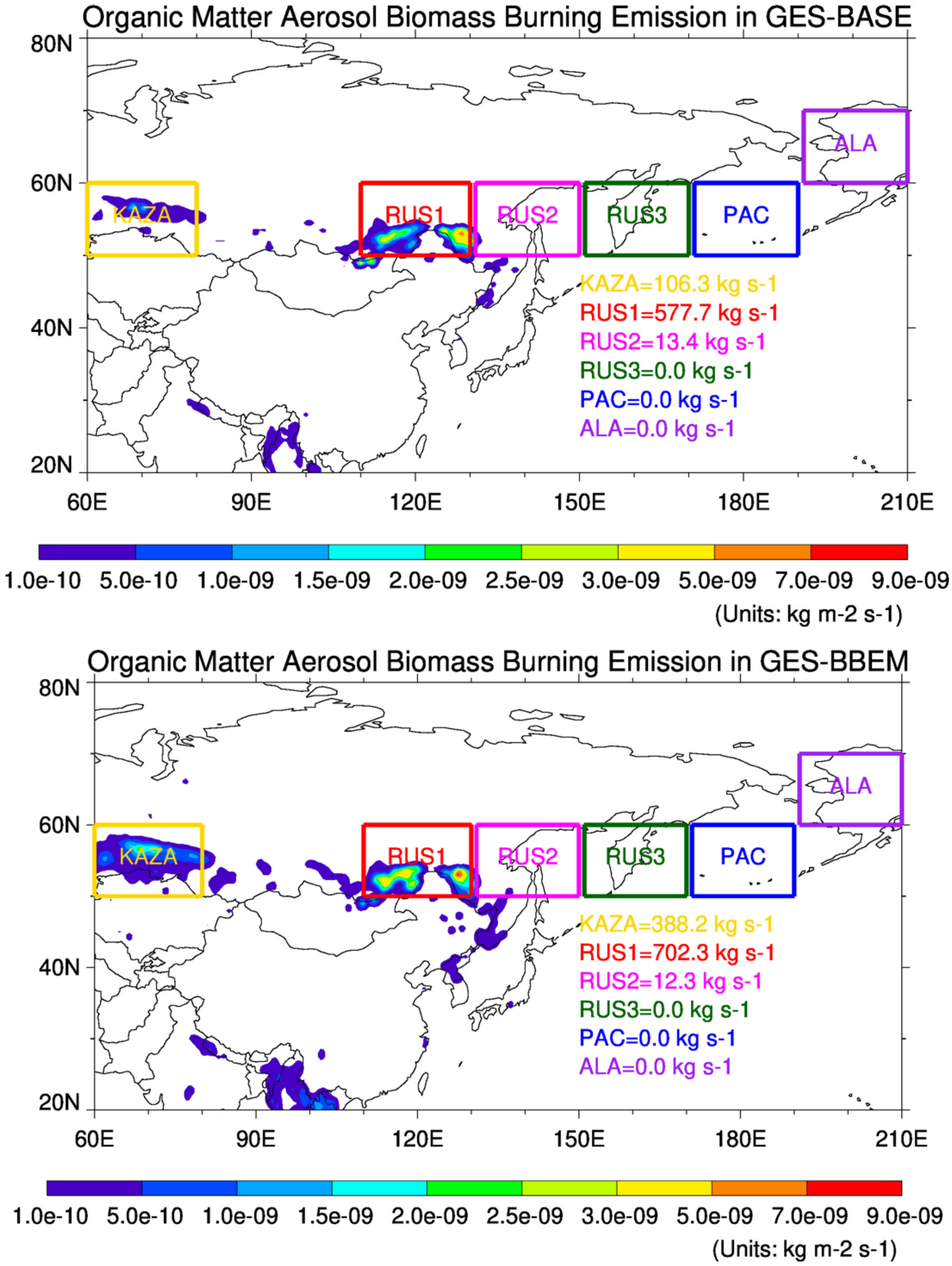

Figure 1. Biomass burning emissions from two inventories. Top: Monthly mean spatial distribution of organic aerosol (OA) emissions from biomass burning in April 2008, based on the GFED4.1s inventory (used in the BASE run), in units of $\mathrm{kg\,m^{-2}\,s^{-1}}$. Bottom: Same as top, but from the FEERv1.0-G1.2 inventory (used in the BBEM run). The six focus regions—KAZA, RUS1, RUS2, RUS3, PAC, and ALA—are outlined and labeled with total emissions.

Smoke Emission Profile derived from MISR in Apr 2008

(a) Percentage of smoke emitted within PBLH

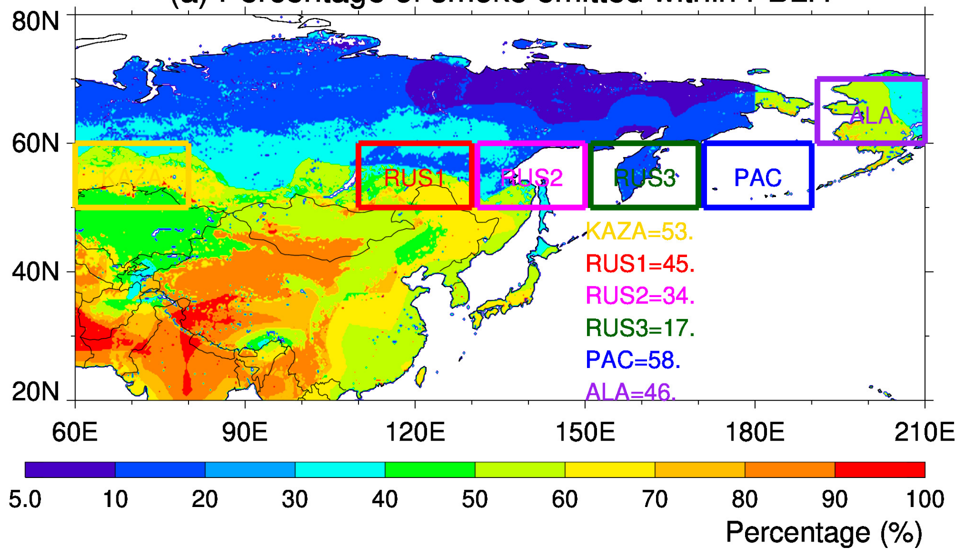

(b) Vertical smoke emission profiles

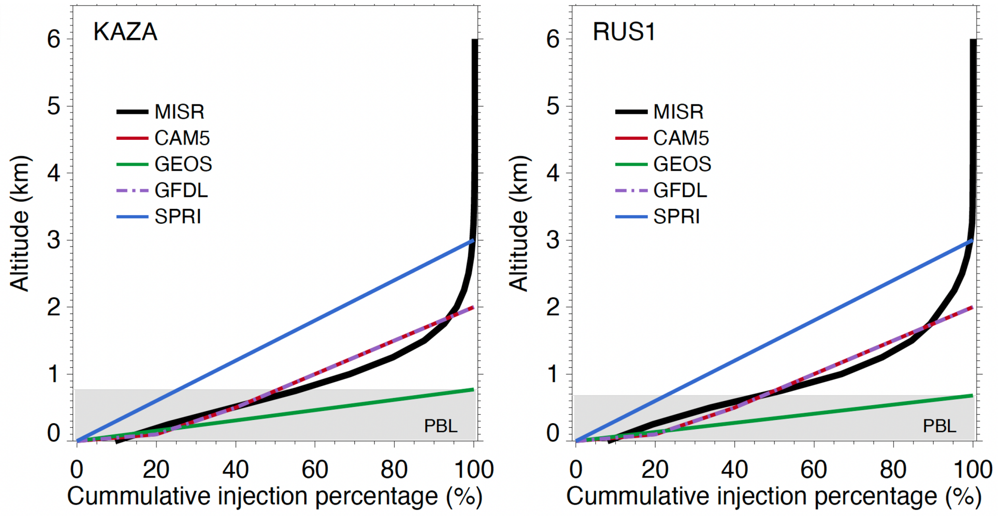

Figure 2. (a) Spatial distribution of the percentage of smoke emitted within the planetary boundary layer (PBL) in April 2008, derived from the MISR- based plume height (units: %), with regional mean values of the six focus regions listed below (over land only). **(b)** Cumulative vertical smoke emission profiles over KAZA and RUS1, with the black thick curve representing the MISR-based plume height used in the BBIH run and the colored curves representing the model default vertical profiles from the models' BASE runs. The PBL layer is shaded in gray.

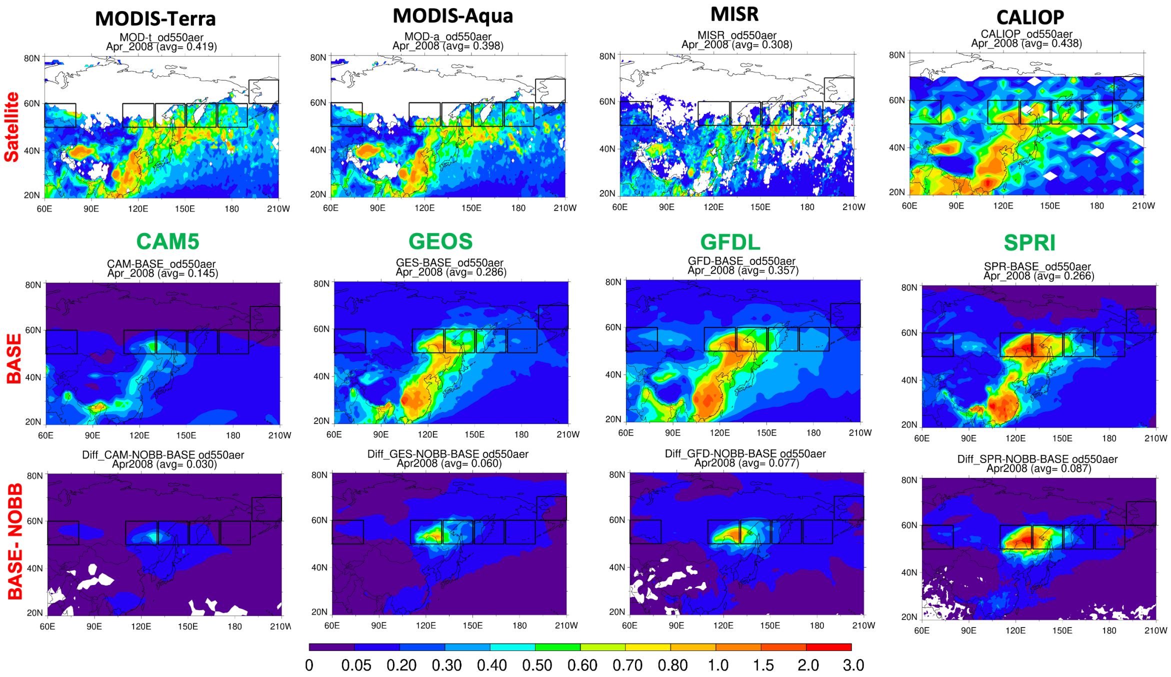

Figure 3a. AOD observations and model simulations**. (a)** Spatial distribution of AOD at 550 nm in April 2008, from four satellite instruments (MODIS-Terra, MODIS-Aqua, MISR, and CALIOP) (Row 1); from four model BASE simulations (CAM5, SPRI, GEOS, and GFDL) (Row 2), and from biomass burning AOD (BASE minus NOBB) (Row 3). Black boxes indicate the six focus regions.

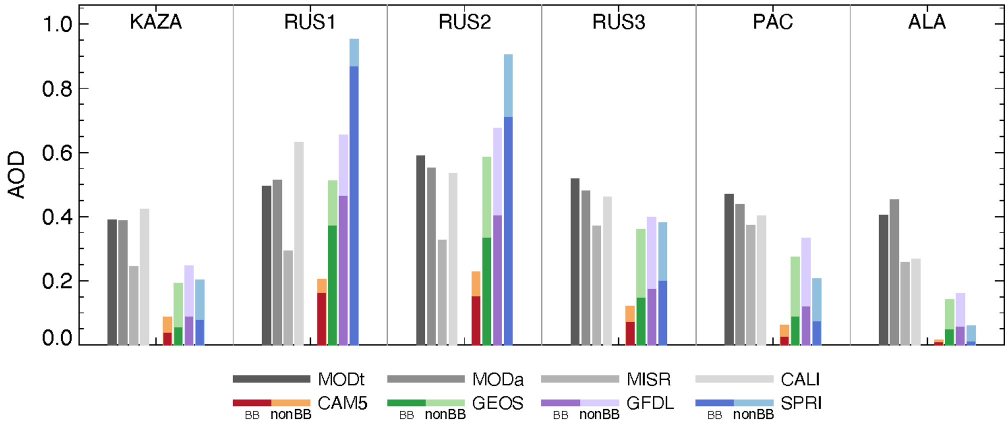

Figure 3b. Regional mean aerosol optical depth (AOD) at 550 nm in April 2008 over the six focus regions (KAZA, RUS1, RUS2, RUS3, PAC, and ALA), derived from four satellite datasets where valid (MODIS-Terra, MODIS-Aqua, MISR, and CALIOP), and from four BASE model simulations (CAM5, SPRI, GEOS, and GFDL). Model AOD values are separated into contributions from biomass burning (BB) and non-biomass burning (nonBB, from NOBB runs).

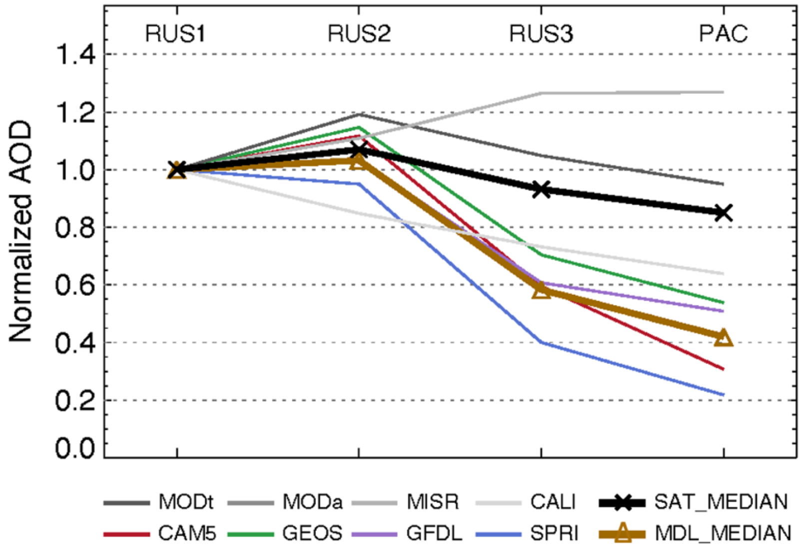

Figure 4. The normalized 550 nm AOD gradient from BB source region RU1 to downwind regions
5 (AOD in all regions normalized to that in RUS1) from satellite observations and the BASE simulations in four regions.

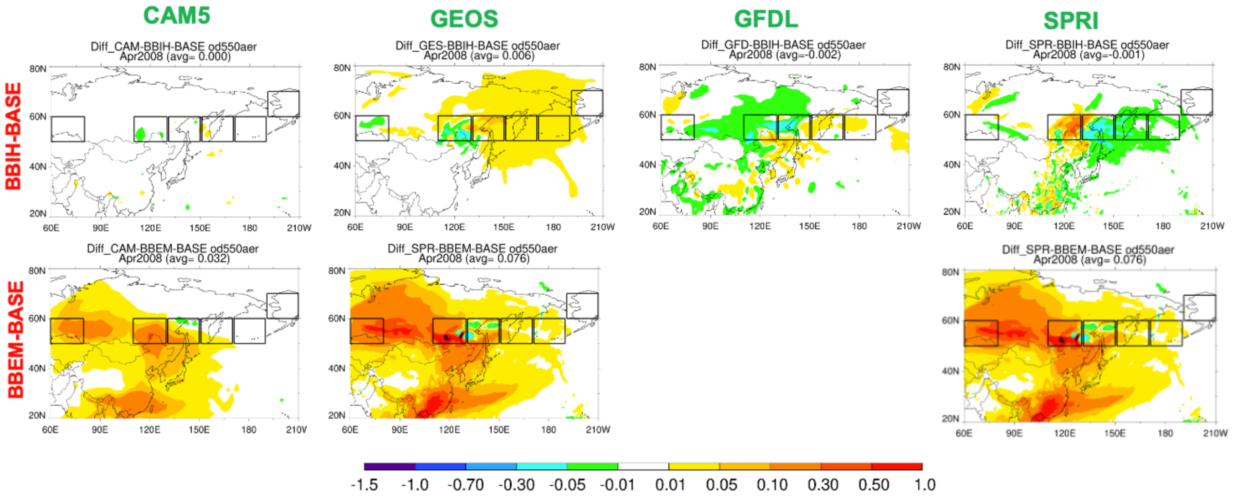

Figure 5a. Spatial differences in AOD at 550 nm between BBIH and BASE (Row 1) and between BBEM and BASE (Row 2), simulated by the four models for April 2008. Only three models—CAM5, GEOS, and SPRI—submitted BBEM simulations. Focus regions are outlined in black.

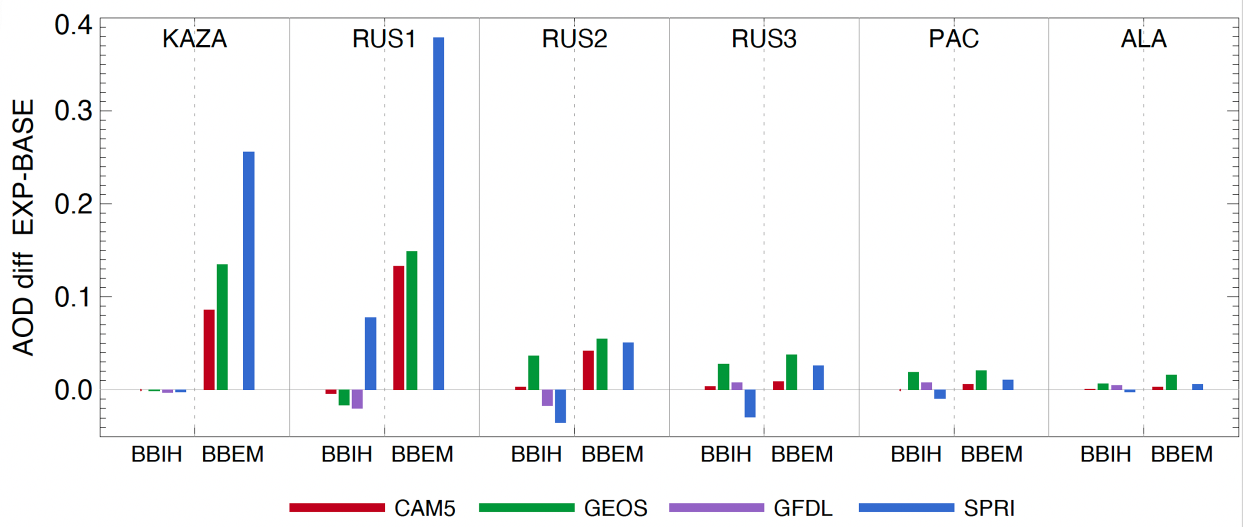

Figure 5b. Regional mean differences in AOD at 550 nm for April 2008 across the six focus regions (KAZA, RUS1, RUS2, RUS3, PAC, and ALA), as simulated by four models (CAM5, SPRI, GEOS, and GFDL). **Left:** BBIH minus BASE; **Right:** BBEM minus BASE. Only three models—CAM5, GEOS, and SPRI—submitted BBEM simulations.

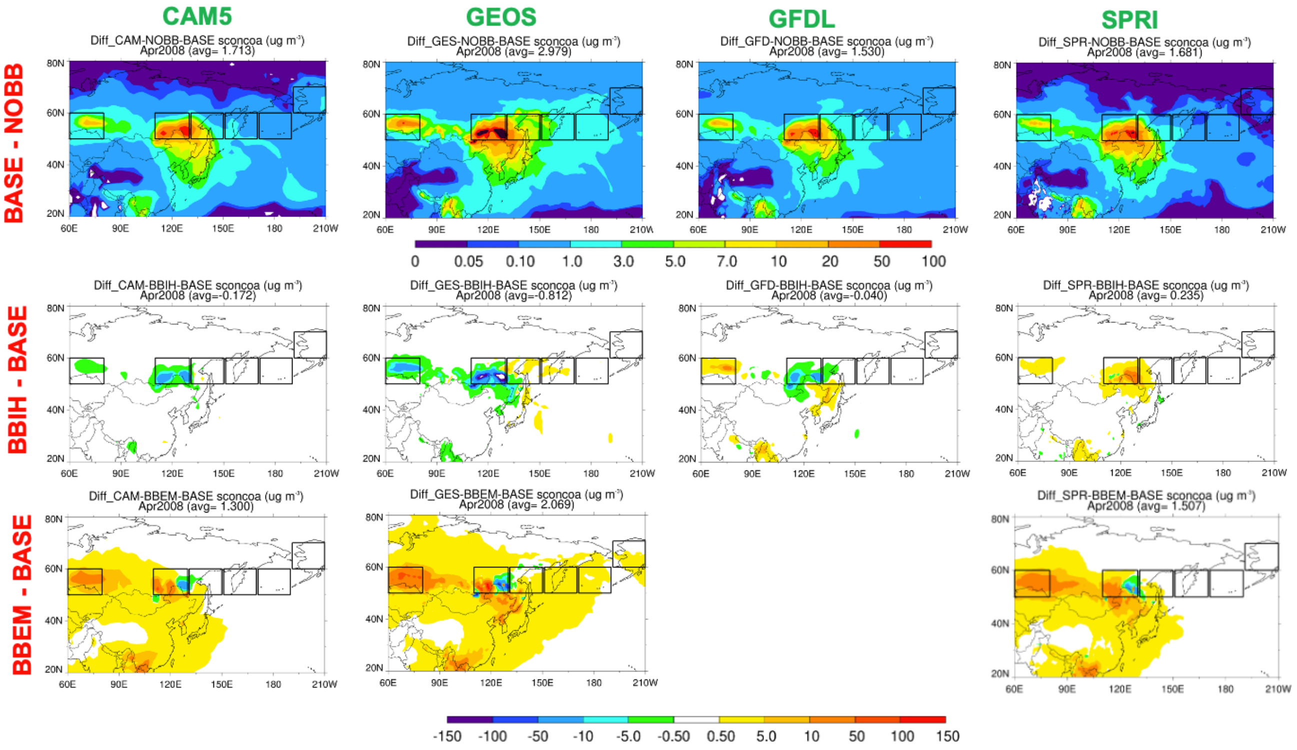

Figure 6. Spatial distribution of differences in surface organic aerosol concentrations for April 2008 across four models: CAM5, SPRI, GEOS, and GFDL. **Row 1:** BASE minus NOBB. **Row 2:** BBIH minus BASE. **Row 3:** BBEM minus BASE. Note that only CAM5, GEOS, and SPRI provided BBEM simulations.

https://doi.org/10.5194/egusphere-2025-2603
Preprint. Discussion started: 30 June 2025

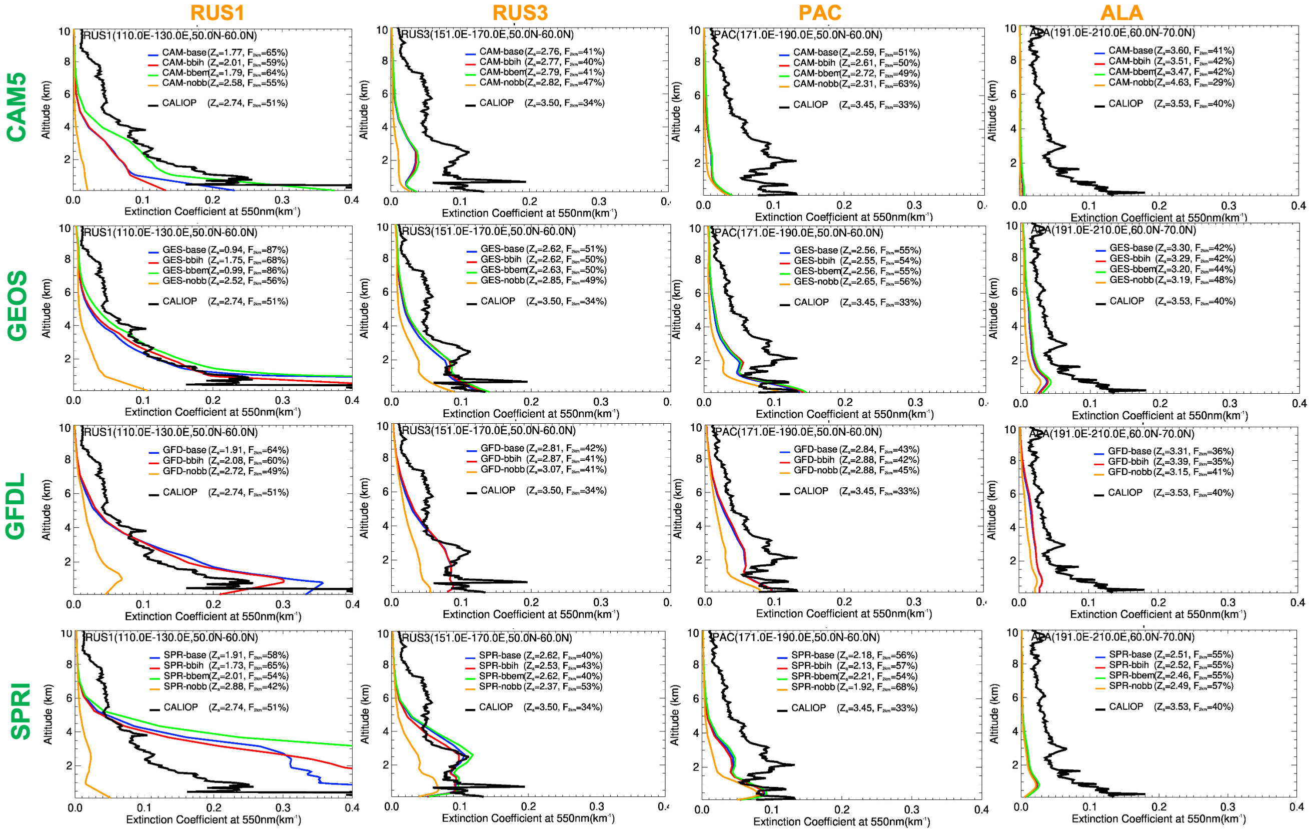

Figure 7. Vertical profiles of aerosol extinction in source and downwind regions. Aerosol extinction profiles for April 2008 from four models (CAM5, SPRI, GEOS, and GFDL), averaged over four regions. **Column 1:** RUS1 (source region); **Columns 2–4:** RUS3, PAC, and ALA (downwind regions). Each panel includes CALIOP observations (thick black curves) and model outputs from four experiments—BASE, BBIH, BBEM, and NOBB—shown as colored curves. Summary statistics are listed beside the legend: Z_a (mean aerosol layer height) and F_{2km} (fraction of AOD within the lowest 2 km.)

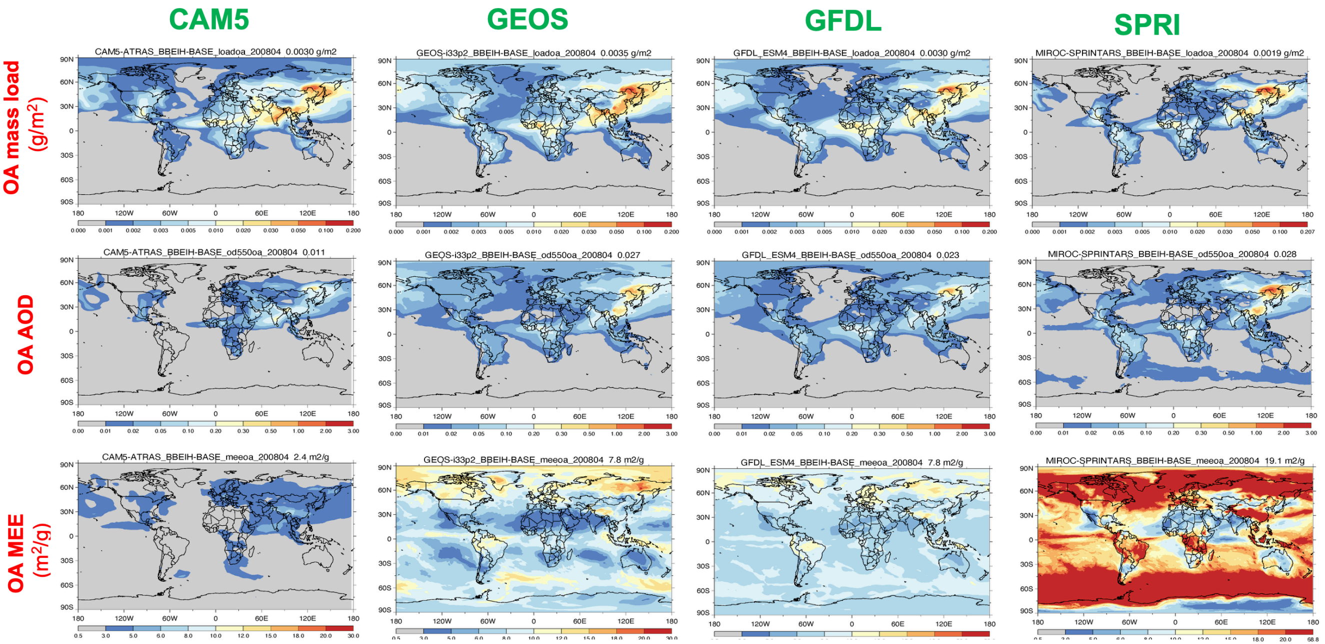

Figure 8. Spatial distribution of OA mass load (units: g m^{-2}), OA AOD, OA mass extinction efficiency (MEE) (units: m^2 g^{-1}) for April 2008, as simulated by four models (CAM5, GEOS, GFDL, and SPRI) in their BASE runs.

https://doi.org/10.5194/egusphere-2025-2603
Preprint. Discussion started: 30 June 2025

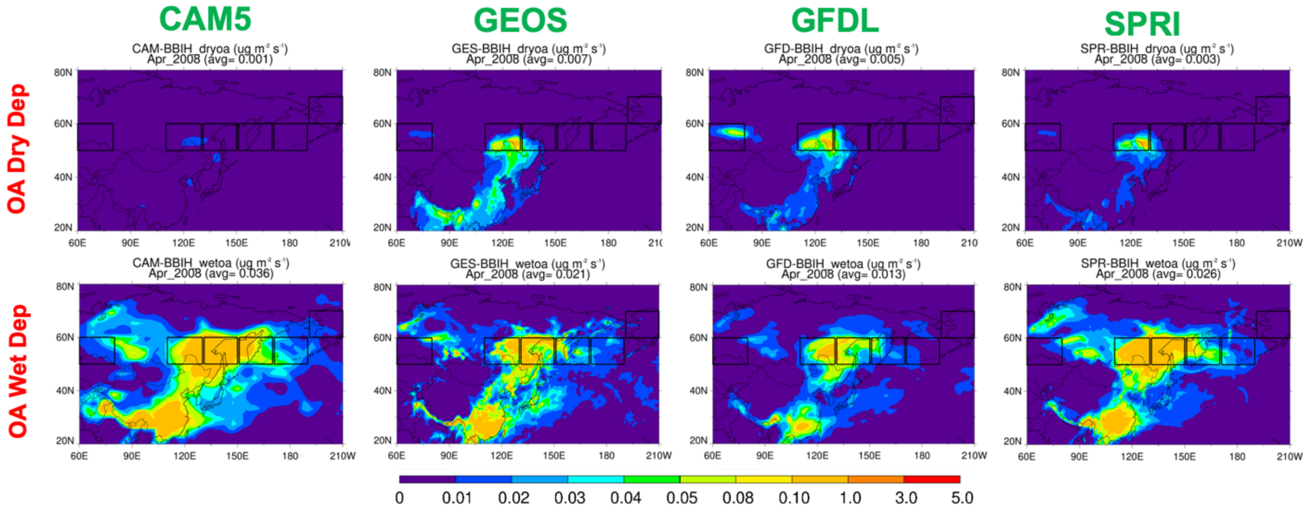

Figure 9. Spatial distribution of OA dry deposition (units: µg m^{-2} s^{-1}) and wet deposition for April 2008, as simulated by four models (CAM5, GEOS, GFDL, and SPRI) in their BBIH runs.